

Effects of a Magnetic Field on Turbulent Flow in the Mold Region of a Steel Caster

RAMNIK SINGH, BRIAN G. THOMAS, and SURYA P. VANKA

Electromagnetic braking (EMBr) greatly influences turbulent flow in the continuous casting mold and its transient stability, which affects level fluctuations and inclusion entrainment. Large eddy simulations are performed to investigate these transient flow phenomena using an accurate numerical scheme implemented on a graphics processing unit. The important effect of the current flow through the conducting solid steel shell on stabilizing the fluid flow pattern is investigated. The computational model is first validated with measurements made in a scaled physical model with a low melting point liquid metal and is then applied to a full-scale industrial caster. The overall flow field in the scale model was matched in the real caster by keeping only the Stuart number constant. The free surface-level behaviors can be matched by scaling the results using a similarity criterion based on the ratio of the Froude numbers. The transient behavior of the mold flow reveals the effects of EMBr on stability of the jet, top surface velocities, surface-level profiles, and surface-level fluctuations.

DOI: 10.1007/s11663-013-9877-x

© The Minerals, Metals & Materials Society and ASM International 2013

I. INTRODUCTION

CONTINUOUS casting (CC) is the predominant method of producing cast steel and is currently used in 95 pct of the world's production.^[1] Because of the large quantities of steel produced, even small improvements in casting quality and defect reduction can result in substantial savings in the unit production cost. The mold region in the CC process contains a complex turbulent flow with large velocities and is responsible for surface defects, slag entrainment and other steel quality problems. The flow at the top surface of the mold can result in hook formation if the velocities are not sufficiently large. However, if the surface velocities are very large, turbulence and shear instabilities can entrain slag from the top surface. If the surface level fluctuates, then the defects can be caused intermittently. Tailoring mold flow provides an opportunity to improve the steel quality. Thus, it is very important to choose nozzle geometries and operating conditions that produce flow patterns within an operating window that avoids these problems.

Operating conditions which control mold flow and related problems include: the mold cross section, casting speed, submergence depth, mold powder, argon gas injection, and electromagnetic forces. The application of a magnetic field is an attractive method to control mold flow because it is nonintrusive and can be adjusted during operation. There are various types of flow control mechanisms using magnetic fields, with a broad classification based on the use of static magnetic fields

using DC current for the electromagnets, or moving fields using AC current. Detailed description of the various types of applied magnetic fields is given in Reference 2. It is well known that the movement of conducting material under the influence of a magnetic field produces a force opposing the motion, and thus should be self-stabilizing. However, the application of a magnetic field can change the flow pattern in non-obvious ways.^[3,4] Understanding how a magnetic field affects the highly turbulent mold flow in CC is both an important and challenging task.

Several previous studies have attempted to understand the flow in the mold region under the influence of different static magnetic field configurations such as local,^[5-9] ruler,^[3,9] and flow-control (FC) mold^[3,10,11] configuration. Cukierski and Thomas^[5] observed that application of local electromagnetic braking (EMBr) weakens the upper recirculation region and decreases the top surface velocity. Harada *et al.*^[9] compared the effects of local and ruler EMBr systems and claimed that both configurations increase surface velocities and dampen high velocities below the mold, and that configuring the ruler configuration below the nozzle ports has better braking efficiency and also results in better surface stability. Li *et al.*^[10] studied the effect of FC mold and reported that with application of the two magnets, one at the meniscus and the second below the nozzle, plug-like flow develops below the mold, and the top surface velocities were so low that the meniscus would be prone to freezing.

As it is difficult to make measurements in real casters, owing to the high temperatures of the molten steel, physical models with other conducting working fluids, such as mercury,^[9] tin,^[10] and eutectic alloys such as GaInSn,^[12-14] have been used in the past to study the effect of magnetic fields. Numerical studies of the mold flow have been extensively used to understand

RAMNIK SINGH, MS Student, and BRIAN G. THOMAS and SURYA P. VANKA, Professors, are with the Department of Mechanical Science and Engineering, University of Illinois at Urbana-Champaign, Urbana IL, 61801. Contact e-mail: bgthomas@illinois.edu
Manuscript submitted April 19, 2013.

the CC process.^[3,5,7,8,14–20] Most of the studies exploring mold flow used Reynolds-averaged Navier–Stokes (RANS)^[3,5,7,8,20,21] or unsteady RANS (URANS)^[14,16] which compute only the mean flow behavior and model the effects of turbulence through turbulence models. However, transient behavior and flow stability is more important to mold flow quality,^[22] yet has received relatively less attention. Direct numerical simulations (DNS) resolves the instantaneous flow accurately but are computationally infeasible at the Reynolds numbers involved in the CC process. On the other hand, large eddy simulations (LES) only model the small scales of turbulence. LES of the mold flow region in CC, without EMB_r^[16,23] and with EMB_r,^[3,17–19] have been performed by a few researchers and were seen to provide a better understanding of the transients involved in the process.

The instantaneous and the mean behaviors of the mold flow are also greatly affected by the electrical conductivity of the solidifying shell.^[10,13,14] Li *et al.*^[10] showed that the incorporation of accurate wall conductivity is necessary as it affects the braking efficiency of the magnetic field. Timmel *et al.*^[13] performed experiments with GaInSn alloy and concluded that with conducting side walls, the mold flow was very stable as opposed to insulated walls with the same magnetic field configuration. Miao *et al.*^[14] conducted URANS simulations of the GaInSn model to study the effects of wall conductivity. However, to our knowledge, there have been no previous studies which performed LES to understand the effects of magnetic fields and wall conductivity on real caster geometries.

In the current study, we have studied the mold flow patterns under the influence of applied magnetic fields incorporating the influence of a conducting shell. An in-house computational fluid dynamics code, CUFLOW, was used to perform LES of the MHD flow in the mold region. The CUFLOW code has been previously validated for several canonical flows such as MHD flows in rectangular ducts^[24,25] and also for the GaInSn model with electrically insulated walls.^[3] In addition, in the current study we use an additional Sub-Grid Scale (SGS) model, called the Coherent-Structure Model (CSM) proposed by Kobayashi,^[26] which incorporates the effect of anisotropy induced by the applied magnetic fields on the filtered scales. The SGS models used in the current study are discussed in detail in Section II–A. The code is first validated by comparing with measurements taken in scaled GaInSn model with conducting brass plates on the wide face walls.^[13] These results are presented in Section IV–A and compared with results for the same model by Chaudhary *et al.*^[3] who performed computations assuming insulated walls. The code is then used to study a full-scale real continuous caster of steel under the influence of a magnetic field. Results for the full-scale caster, with and without the applied magnetic field, are presented in Section V. The time-averaged and instantaneous flows, Reynolds stresses, turbulent kinetic energy (TKE), surface-level profiles, and surface-level fluctuations are computed to study the effects of ruler EMB_r on the details of the flow phenomena and similarity criteria for scaleup.

II. GOVERNING EQUATIONS FOR LES OF MHD FLOW

In the current study, we solve the unsteady three-dimensional filtered Navier–Stokes (N–S) equations and the filtered continuity equation given by Eqs. [1] and [2], respectively. The effects of the flow phenomena too small to be captured by the grid spacing, and thus spatially filtered, are incorporated by an eddy viscosity (ν_s) which is modeled by a SGS model.

$$\frac{\partial u_i}{\partial t} + \frac{\partial u_i u_j}{\partial x_j} = -\frac{1}{\rho} \frac{\partial p^*}{\partial x_i} + \frac{\partial}{\partial x_j} \left((\nu + \nu_s) \left(\frac{\partial u_i}{\partial x_j} + \frac{\partial u_j}{\partial x_i} \right) \right) + \frac{1}{\rho} F_i \quad i = 1, 2, 3 \quad (1)$$

$$\frac{\partial u_j}{\partial x_j} = 0 \quad (2)$$

where i, j imply tensor notation, and repeated indices in a term indicate summation, u_i are the three velocity components, p^* is the pressure modified to include the filtered normal stresses ($p^* = p + (1/3)\rho\tau_{kk}$), where p is the static pressure, ρ is the fluid density, ν is the kinematic viscosity, and F_i in Eq. [1] represents the three Lorentz-force components.

The molten steel flowing through the magnetic field generates an electric current (\vec{J}), which flows through the entire domain producing the Lorentz force (\vec{F}), and is given by

$$\vec{J} = \sigma(\vec{E} + \vec{u} \times \vec{B}_0) = \sigma(-\vec{\nabla}\phi + \vec{u} \times \vec{B}_0) \quad (3)$$

This equation has been obtained after neglecting the induced magnetic field which is usually small compared with the applied magnetic field.^[27] The charge conservation condition, $\nabla \cdot \vec{J} = 0$, is then used to get an equation for the potential ϕ .

$$\nabla \cdot (\sigma \nabla \phi) = \nabla \cdot (\sigma(\vec{u} \times \vec{B}_0)) \quad (4)$$

The Lorentz force (\vec{F}) is given by

$$\vec{F} = \vec{J} \times \vec{B}_0 \quad (5)$$

Here σ is electrical conductivity, \vec{E} is induced electric field, ϕ is electric potential, and \vec{B}_0 is the applied magnetic field.

This set of coupled MHD equations is solved by a finite volume method and implemented on a graphics processing unit (GPU) for fast computation. The numerical details of solving these equations have been discussed in previous studies^[3,24,25,28,29] and hence are only briefly described in Section III–B.

A. Sub-Grid Scale (SGS) Models

The effects of the turbulent flow scales, too small to be captured by the computational grid, are incorporated by SGS models. With increase in grid refinement, contribu-

tion of the SGS model diminishes such that the modeled eddy viscosity eventually tends to zero as the refinement nears the requirements of a DNS. One of the earliest and the simplest of the SGS models is the Smagorinsky model,^[30] in which the SGS eddy viscosity is calculated as

$$\nu_s = (C_s \Delta)^2 |\bar{S}| \quad [6]$$

where C_s is the Smagorinsky constant, Δ is the grid cell volume, and $|\bar{S}|$ is the magnitude to the velocity strain tensor $S_{ij} = \frac{1}{2} \left(\frac{\partial u_i}{\partial x_j} + \frac{\partial u_j}{\partial x_i} \right)$. In the current study, two variants of the Smagorinsky SGS models were used, as described in the following sections.

1. Wall-Adapting Local Eddy-viscosity (WALE) Model

The WALE model^[31] calculates the eddy viscosity with appropriate scaling to insure a near-zero value close to the walls: (αy^3) . This is a favorable feature for studies involving confined flows. The eddy viscosity is calculated as

$$\nu_s = L_s^2 \frac{(S_{ij}^d S_{ij}^d)^{3/2}}{(S_{ij} S_{ij})^{5/2} + (S_{ij}^d S_{ij}^d)^{5/4}} \quad [7]$$

where $S_{ij}^d = \frac{1}{2} (g_{ij}^2 + g_{ji}^2) - \frac{1}{3} \delta_{ij} g_{kk}^2$, $g_{ij} = \frac{\partial u_i}{\partial x_j}$, $L_s = C_w (\Delta x \Delta y \Delta z)^{1/3}$, $C_w^2 = 10.6 C_s^2$, $C_s = 0.18$, and Δx , Δy , and Δz are the grid spacings in x , y , and z directions, respectively.

2. Coherent-structure Smagorinsky (CSM) Model

The CSM SGS model^[32] dynamically calculates the model parameter: (C) and has been shown to accurately predict the relaminarization of a turbulent flow subjected to a strong magnetic field. The CSM model incorporates the anisotropic effects of the applied magnetic field and also damps the eddy viscosity close to the wall by dynamically calculating the model constant. The model constant is calculated using a coherent-structure function (\mathcal{F}_{CS}) as shown in Eqs. [8] through [11].

$$C_s^2 = C = C_{CSM} |\mathcal{F}_{CS}|^{3/2} \mathcal{F}_\omega \quad [8]$$

$$C_{CSM} = \frac{1}{22}, \quad \mathcal{F}_{CS} = \frac{Q}{E}, \quad \mathcal{F}_\omega = 1 - \mathcal{F}_{CS} \quad [9]$$

$$W_{ij} = \frac{1}{2} \left(\frac{\partial u_j}{\partial x_i} - \frac{\partial u_i}{\partial x_j} \right) \quad [10]$$

$$Q = \frac{1}{2} (W_{ij} W_{ij} - S_{ij} S_{ij}) \quad E = \frac{1}{2} (W_{ij} W_{ij} + S_{ij} S_{ij}) \quad [11]$$

III. COMPUTATIONAL MODEL

A. Computational Domain, Mesh, and Boundary Conditions

Two different flow geometries were investigated in the current study: a scaled low-melting point liquid-metal

(GaInSn) model with a ruler EMBr field, and a corresponding full-scale caster, six-times larger in every dimension. Figure 1 gives the geometric details, with dimensions corresponding to the real caster domain, with the sectioned region representing the solidified steel shell on the walls of the real caster mold. The maximum field strength of the ruler EMBr is positioned across the nozzle outlet ports, centered 92 mm below the free surface of the liquid metal in the scale model, and 552 mm ($= 6 \times 92$ mm) in the real caster. The variations of the applied magnetic field within the mold for both the GaInSn model and the real caster are shown in Figure 2. Dimensions, process parameters, and material properties for both geometries are provided in Table I.

The GaInSn model has been experimentally studied with no magnetic braking (Case 1),^[12] magnetic braking with insulated walls (Case 2),^[12] and magnetic braking with conducting walls (Case 3).^[13] Miao *et al.*^[14] modeled all the three cases with URANS. Chaudhary *et al.*^[3] validated CUFLOW with measurements for Case 1 and Case 2, and also studied the flow features in detail. Case 3, which has conducting brass-plated wide-faced walls, also was simulated in the current study to validate the model by comparing the results with measurements, and also to investigate the effects of wall conductivity.

For the real caster domain, simulations with no EMBr (Case 4) and with EMBr (Case 5) were performed. The computational domain for the real caster included both the liquid pool, shown in Figure 3, and the solidifying shell, which was initialized to move in the casting direction at the casting speed. The shell thickness s at a given location below the meniscus was calculated from $s = k\sqrt{t}$, where t is the time taken by the shell to travel the given distance and the constant k was chosen to match the steady-state shell profile predicted from break-out shell measurements by Iwasaki and Thomas.^[33] The scaling factor of six over the GaInSn model was chosen to have mold dimensions typical of a commercial continuous slab caster. In the absence of EMBr, previous studies^[34] have found that the Froude similarity criterion matches the flow patterns between a real caster and a $1/3^{\text{rd}}$ scaled water model. In a previous study with EMBr in a scaled mercury model,^[9] Froude number ($Fr = U/\sqrt{gL}$) and Stuart number ($N = B_0^2 L \sigma / \rho U$) similarity criteria were simultaneously maintained by scaling the casting speed and the magnetic field strength. Froude number maintains the ratio between inertial and gravitational forces, whereas Stuart number maintains the ratio between electromagnetic and inertial forces. However, in the current study, only the Stuart number was matched between the $1/6^{\text{th}}$ scaled GaInSn model and the corresponding real caster, keeping the magnetic field strength constant at the realistic maximum of 0.31 Tesla. Maintaining Froude similarity as well would have required a very high casting speed of 3.3 m/min, and a higher magnetic field strength of 0.44 Tesla. The applicability of this scaleup criterion was investigated by comparing the results for the scale model with the real caster with EMBr.

The GaInSn and the real caster computational meshes consist of 7.6 and 8.8 million brick cells, respectively. The nozzle in the physical model was very long

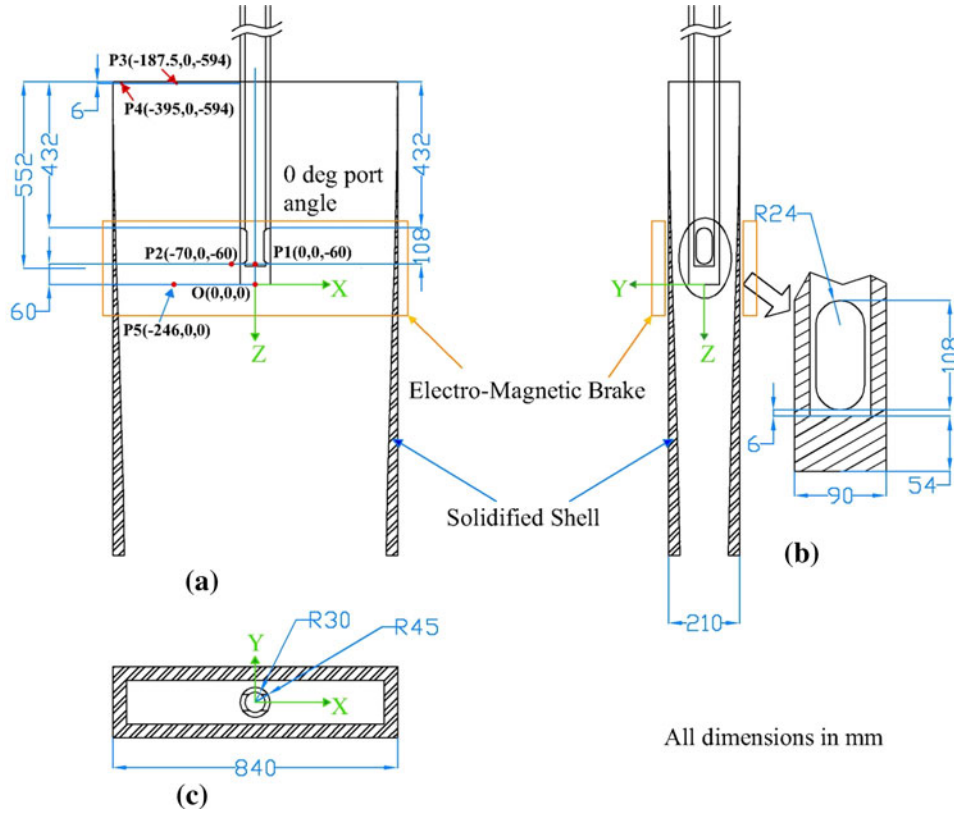


Fig. 1—Geometry of the real caster with the rectangle showing the location of the applied ruler EMBR.

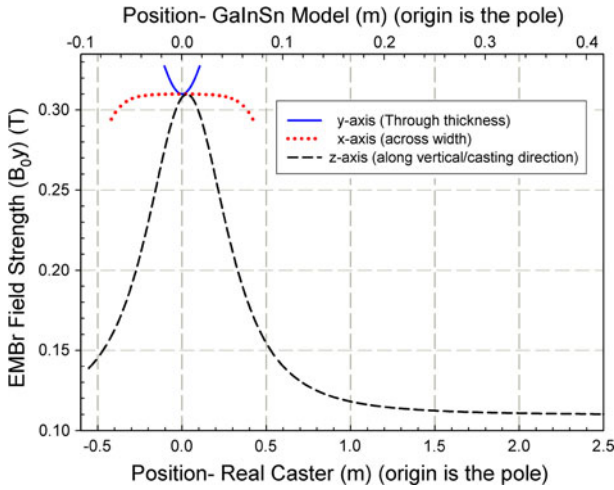


Fig. 2—Applied magnetic field in the x, y, and z directions for GaInSn model and real caster.

(20 diameters), and hence, the nozzle inlet flow conditions had no effect on the flow entering the mold. Thus, in the computational model, the nozzle was truncated at the level of the liquid surface in the mold and a fully developed turbulent pipe flow velocity profile (Eq. [12]) was applied at the inlet, as used in previous studies.^[3,16]

$$V_z(r) = V_z^{\text{centerline}} \left(1 - \frac{r}{R}\right)^{\frac{1}{2}} \quad [12]$$

where $V_z(r)$ is the mean velocity in the casting direction as a function of r , which is the distance from the center of the circular nozzle inlet, and R is the radius of the nozzle. The top free surface in the mold was a free-slip boundary with zero normal velocity and zero normal derivatives of tangential velocity. A convective boundary condition (Eq. [13]) was applied to all three velocity components at the two mold outlet ducts on the narrow faces (NF) in the case of the scaled model^[16] and across the open bottom of the real caster domain

$$\frac{\partial u_i}{\partial t} + U_{\text{convective}} \frac{\partial u_i}{\partial n} = 0 \quad i = 1, 2, 3 \quad [13]$$

where $U_{\text{convective}}$ is the average normal velocity across outlet plane, and n is the direction normal to the outlet plane.

All other boundaries were solid walls, and the wall treatment previously reported by Werner and Wengle^[35] was applied. In the real caster, the boundaries between the shell and fluid regions were initialized with fixed downward vertical velocity equal to the casting speed, which accounts for mass transfer from the fluid region to the solidifying shell. Insulated electrical boundary condition ($\frac{\partial \phi}{\partial n} = 0$) was applied on the outer-most boundary of the computational domain. The fluid flow equations were solved only in the fluid domain, and the MHD equations were solved in the entire computational domain, including the brass walls for the GaInSn

Table I. Process Parameters

	GaInSn Model	Real Caster
Volume flow rate nozzle bulk inlet velocity	110 mL/s 1.4 m/s	4.8 L/s 1.7 m/s
Casting speed	1.35 m/min	1.64 m/min
Mold width	140 mm	840 mm
Mold thickness	35 mm	210 mm
Mold length	330 mm	1980 mm
Computational domain length	330 mm	3200 mm
Nozzle port dimensions (width × height)	8 × 18 mm ²	48 × 108 mm ²
Nozzle bore diameter (inner outer)	10 mm 15 mm	60 mm 90 mm
SEN submergence depth (liquid surface to top of port)	72 mm	432 mm
Thickness of shell on the wide faces	0.5 mm	$s \text{ (mm)} = 2.75\sqrt{t(s)}$
Thickness of shell on the narrow faces	0 mm	$s \text{ (mm)} = 2.75\sqrt{t(s)}$
Fluid material	GaInSn eutectic alloy	Molten steel
Viscosity	$0.34 \times 10^{-6} \text{ m}^2/\text{s}$	$0.86 \times 10^{-6} \text{ m}^2/\text{s}$
Fluid density	6360 kg/m ³	7000 kg/m ³
Conductivity of liquid (σ_{liquid})	$3.2 \times 10^6 \text{ 1}/\Omega\text{m}$	$0.714 \times 10^6 \text{ 1}/\Omega\text{m}$
Conductivity of walls (σ_{wall})	$15 \times 10^6 \text{ 1}/\Omega\text{m}$	$0.787 \times 10^6 \text{ 1}/\Omega\text{m}$
Conductivity ratio (C_w)	0.13	0.13
Nozzle port angle	0 deg	0 deg
Gas injection	No	No
Reynolds number (Re , based on nozzle diameter)	41,176	118,604
Hartmann number ($Ha = BL\sqrt{\sigma/\rho\nu}$, based on mold width)	1670	2835
Froude number ($Fr = U/\sqrt{gL}$, based on mold width)	1.19	0.59
Stuart number ($N = B_0^2 L \sigma / \rho U$, based on mold width)	4.84	4.84
Cases	1. No-EMBr 2. EMBr with insulated walls 3. EMBr with conducting walls	4. No-EMBr 5. EMBr with conducting walls

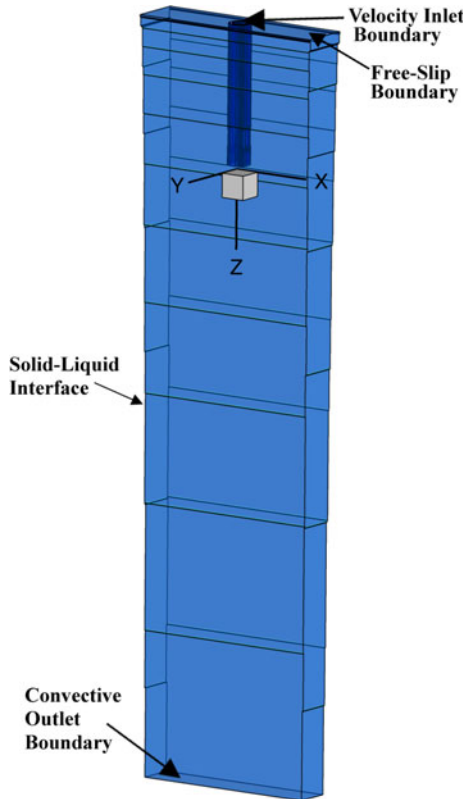


Fig. 3—Isometric view of the computational domain (fluid flow region) for the real caster.

domain and the shell (shaded) region for the real caster domain.

B. Numerical Method and Computational Cost

An in-house code, CUFLOW, was used in the current study which solves the coupled N–S and MHD equations (Eqs. [1] through [5]) on a structured Cartesian grid. This code uses a fractional step method for the pressure–velocity coupling and the Adams–Bashforth temporal scheme and second-order finite volume method for discretizing the momentum equations. The pressure Poisson equation (PPE) and the electric Poisson equation (EPE) (Eq. [4]) are solved using a geometric multigrid solver. The cases without the EMBr field were started with a zero initial velocity whereas the EMBr cases were started from a developed instantaneous flow field from a simulation with no magnetic field.

For the GaInSn model, the magnetic field was applied after 10 seconds of simulation time (200,000 time steps) for the conditions of Case 1. The flow field for Case 3 was then allowed to develop for 5 seconds before starting to collect the time averages. The time-averaged quantities were stabilized for 2 seconds after which the turbulence statistics were collected for 10 seconds. This simulation required a total of 10 days of calendar computation time. The real caster simulation was also started first with zero initial velocity and no magnetic field (Case 4). The collection of time averages was

started after 10 seconds (200,000 time steps) and the turbulence quantities were calculated after the means stabilized for 5 seconds. The turbulence quantities were then averaged for another 15 seconds, requiring a total of 10 days computing time. For the case with EMBr (Case 5), the developed no EMBr flow field was taken as a starting condition, and the flow was allowed to stabilize for 10 seconds physical time before calculating the time-averaged quantities. The turbulence quantities were then calculated after the time-averaged quantities were stabilized for 5 seconds of physical time after which further averaging for 10 seconds was performed. This calculation required a total of 15 days computation time.

The computations were performed on a NVIDIA C2075 GPU with 1.15-GHz cuda-core frequency and 6-GB memory. The solution times for the EMBr cases were nearly double that of the cases without EMBr, which also require the solution of the EPE. The calculations with EMBr produced approximately 55,000 time steps per day for the GaInSn model and approximately 35,000 time steps per day for the real caster. The computational expenses due to a larger grid size and double precision accuracy in the real caster cases required larger computing time per time step.

IV. RESULTS FOR THE GaInSn SCALED MODEL

A. Comparison with Experimental Measurements

Measurements of time-varying horizontal velocity (V_x) in the GaInSn model were collected at 5 Hz using an array of ten ultrasonic Doppler velocimetry (UDV) sensors.^[12,13] The first sensor was placed at $z = -40$ mm on the midplane of the NF, and the subsequent ones were placed at 10-mm intervals below the first. Figure 4(a) shows the contour plot of measured time-averaged horizontal velocity.^[12,13] The plot on the top is for the insulated wall case, whereas the lower plot is for the conducting wall case. Figure 4(b) shows the contour plot of the same quantity calculated using CUFLOW for both cases. However, here the vertical resolution was matched with the experimental data by using the calculated values on ten horizontal lines with positions matching those of the UDV sensors in the experimental setup. Figure 4(b) shows a good qualitative match with the measurements for both the insulated and conducting wall cases. Figure 4(c) shows the contour plots of the same calculated quantity for both cases but with a much higher data resolution, using all computational grid points. In this plot, the entire jet region is visualized by a continuous region of high velocity unlike the previous plots. The low vertical resolution, used in the measurements, results in graphical artifacts such as two isolated regions of high velocity in each jet. The plots shown in Figure 4(b) help in comparing the calculated results with the plots obtained from the measurements, which exhibit almost exactly the same respective flow fields, including the two high-velocity regions in each jet. However, the higher-resolution contour plots of the same data look

considerably different from the low-resolution contour plots.

The application of a ruler magnetic field is known to deflect the jet upward,^[3] and a similar behavior is seen in the simulation with conducting walls. The time-averaged horizontal velocity shows that the jet angles for both conducting and insulated cases are nearly the same, but the conducting wall case shows less spreading of the jet, before it impinges on the NF, compared with the insulated wall case. Also, for the conducting case, strong recirculation regions were seen, just above and below the jet (negative velocity implies flow toward the NF). This contrasts with the insulated wall case, in which very strong recirculating flow is seen only above the jet. Both flow fields are in contrast to that without EMBr (presented later) where no recirculation is seen in this zoomed-in portion of the domain.

Figure 5 compares the measured and calculated time-averaged horizontal velocities on three horizontal lines, 90, 100, and 110 mm from the free surface (corresponding to the 4th, 5th and 6th sensors) for the case with conducting walls. Results computed using both the WALE SGS model and the CSM SGS model are shown. For the current case, both models give results which closely match the measurements, but the CSM SGS model is expected to perform better for the real caster because of the higher Reynolds number and larger fraction of the energy in the filtered scales. Further, the large Stuart number, 4.84, induces anisotropy of the turbulence^[36] which is better represented by the CSM SGS model. Thus, henceforth, only those results with only the CSM SGS model are shown. The agreement between the measurements and the calculations is very good except close to the SEN and NF walls, which is primarily due to limitations in the UDV measurements. Timmel *et al.*^[12,13] report that the UDV measurements are inaccurate near the SEN and the walls because of the low vertical spatial resolution and the interaction of the ultrasonic transducer beam with solid surfaces.

The transient horizontal velocities measured by the UDV probes were compared with the calculations at a point in the jet region, P5 ($x = -41$ mm, $y = 0$ mm, $z = 0$ mm), in Figure 6(b). In order to match the conditions of the transient measurements closely, a 0.2-second time average was performed on the calculated signal to match the response frequency (5 Hz) of the measuring instrument.^[13] The measured and the time-averaged signals match well.

B. Instantaneous Results

The flow pattern for the EMBr case with insulated walls (Case 2) was remarkably different from the same case with conducting walls (Case 3). The transient differences are even greater. Figure 6(a) shows the history of horizontal velocity for Case 2 at P5, a typical point in the jet, which contrasts greatly with the history in Figure 6(b) for Case 3 at the same location. The insulated wall case has strong low-frequency fluctuations which indicate large scale wobbling of the jets. This behavior is not seen in the conducting wall case. The contrasting transient behaviors are clearly visualized in

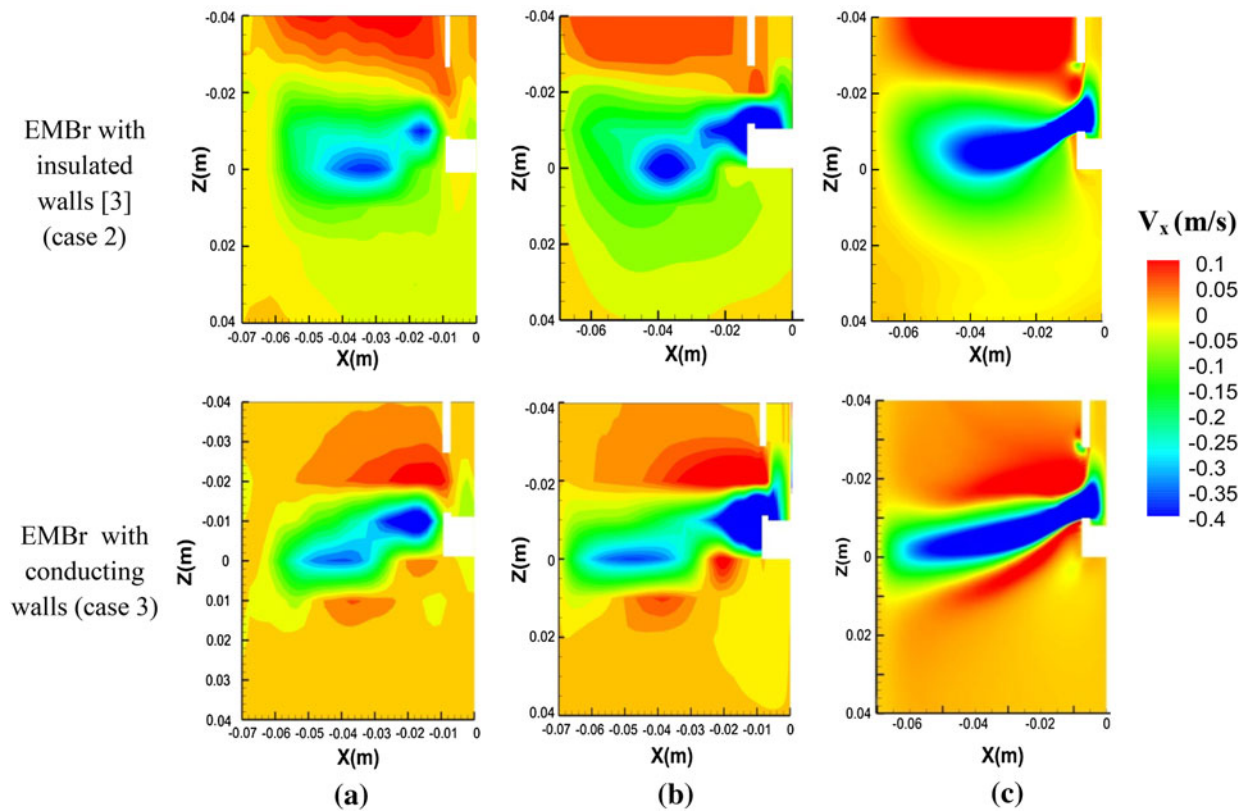


Fig. 4—Contours of time-averaged horizontal velocity for case 2 (top) and case 3 (bottom) for the GaInSn model caster. (a) Measurements; (b) and (c) calculations using CUFLOW.

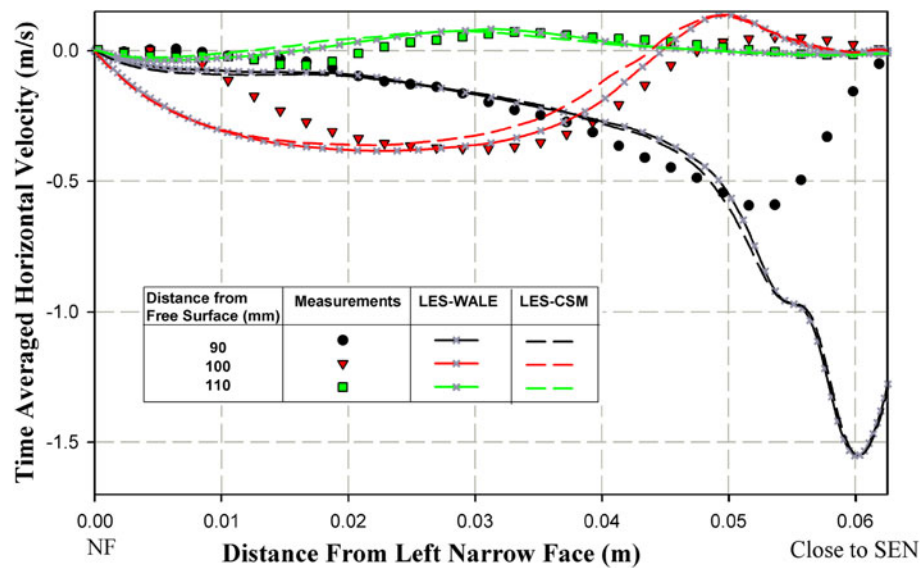


Fig. 5—Comparison of time-averaged horizontal velocity between measurements and CUFLOW calculations using WALE SGS model and CSM SGS model for the GaInSn model caster with conducting walls (case 3).

Figure 7, which show contour plots of instantaneous velocity magnitude at the midplane between wide faces at two instances, separated by 2 seconds, for both cases. Case 2 has both side-to-side and up-and-down wobbling of the jets, which makes the entire mold flow very unstable; whereas the jet in Case 3 is relatively stable.

Figure 7 also shows the contours of time-averaged velocity magnitude for both cases (leftmost column). Case 2 has an asymmetric flow pattern even after collecting the mean for 28 seconds, whereas the calculations with conducting walls (Case 3) produced a symmetric time-averaged velocity field after averaging

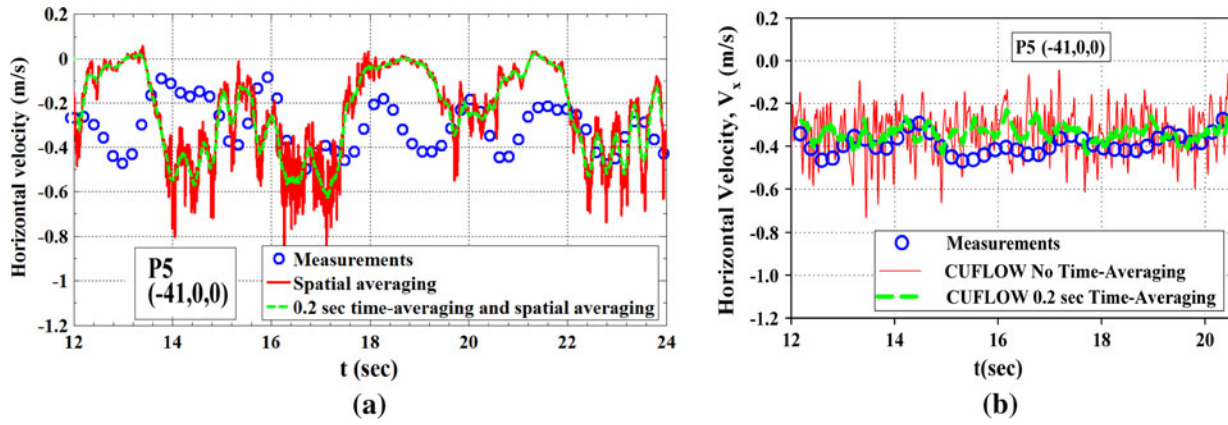


Fig. 6—Transient horizontal velocity in the jet comparing CUFLOW predictions and measurements in the GaInSn model (a) EMBR with insulated walls^[3] and (b) EMBR with conducting walls.

for only 12 seconds. This finding of increased flow stability with conducting walls, and the contrast of very unstable flow with insulated walls,^[3] agrees with previous findings using both experiments and URANS models.^[13,14]

The change in the flow pattern in the presence of the conducting walls can be explained by the behavior of the current paths.^[14] In the case with insulated walls (Case 2), the current lines may close either through the conducting-liquid metal or the Hartmann layers (present on walls perpendicular to the magnetic field). The Hartmann layers are extremely thin ($\sim 40 \mu\text{m}$ in Case 3^[14]) at high Ha number ($\delta_{Ha} \sim Ha^{-1}$), resulting in high resistance, and thus most of the return current closes through the liquid metal itself. The enhanced stability of the mold flow in case with conducting walls (Case 3) is enabled by the alternative path provided to the current through the conducting walls. Most of the current is generated in the jet region and closes locally through the conducting wall, forming short loops where the magnetic field is strongest. This prevents the current from wandering through the flow, where it can generate strong transient forces causing the unstable flow as seen with insulated walls. Figure 8(a) shows the time-averaged current paths in the regions of the mold with maximum current for Case 3. These current loops are the most important because they produce the maximum Lorentz forces acting on the flowing metal. Most of the current paths can be seen to go up and through the jet, travel to the conducting walls, move down through the conducting walls (where they are colored gray) and then back to the jet. Figures 8(b) and (c) show contour plots of time-averaged current density magnitude for Case 3 with vectors in the y - z plane at $x = -12 \text{ mm}$ (slice through the jet) and x - y plane at $z = -10 \text{ mm}$ (slice through the SEN ports), respectively. Figure 8(b) shows that the maximum current density occurs within the conducting walls near to the nozzle bottom, while within the fluid, the maximum is associated with the jet, near where high-velocity fluid intersects with the maximum field strength. Figure 8(c) shows that there is high current density in the conducting walls all across the width of the mold at $z = -10 \text{ mm}$. More importantly,

the highest current densities in the fluid region are found inside and just outside the nozzle ports, decreasing toward the NFs.

C. Time-Averaged Results

1. Nozzle flow

Figures 9(a) and (b) show the time-averaged velocity magnitude and vectors at the nozzle port for the No-EMBr (Case 1) and EMBR (Case 3) cases, respectively. It can be seen that the time-averaged velocity magnitudes are symmetric in the jet region near nozzle port exit for both cases indicating adequate sample size. The jet in the presence of the EMBR (Case 3) was deflected upward and was also much thinner compared with the No-EMBr case. There were two strong recirculation regions, above and below the jet, which return the jet fluid close to the jet exit.

The application of magnetic fields is known to suppress turbulent fluctuations.^[27] This effect is shown in Figure 11 where the $\overline{w'w'}$ component of resolved Reynolds stresses is plotted inside the nozzle in the midplane parallel to the NFs. The No-EMBr case has the larger fluctuation levels and hence sustains swirl in the z - y plane which was evident from the high values of the $\overline{w'w'}$ and $\overline{v'v'}$ (not shown) components. The EMBR configuration applies a high strength of magnetic field in the nozzle region which almost completely suppresses the swirl. The suppression was, however, found to be lesser in the conducting wall case. Thus, another contributing factor to the stability of the mold flow pattern for the conducting wall case was the better mixing present in the nozzle, as swirling jet flow is known to improve jet stability.

2. Mold flow

Figure 10(a) shows the contours of time-averaged velocity magnitude and vectors in the mold for the No-EMBr case. Figure 10(b) also shows the contours of time-averaged velocity magnitude for the EMBR case with conducting walls but with streamlines instead of vectors. Due to the recirculating regions and high gradients close to the jets the vectors masked most of

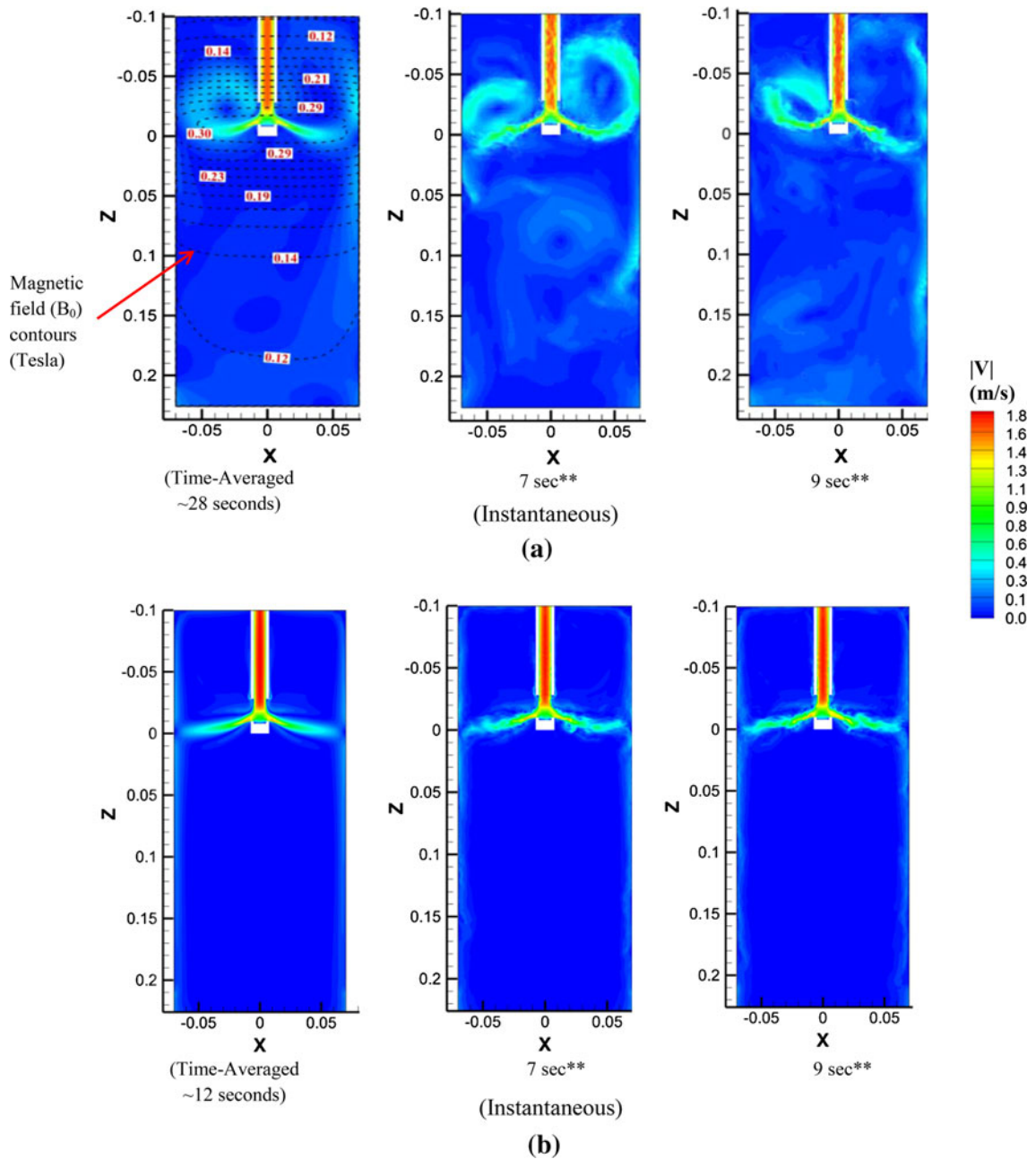


Fig. 7—Time-averaged and instantaneous velocity magnitude (a) EMBr with insulated walls^[3] and (b) EMBr with conducting walls (**time after switching on EMBr) (all axes in meters).

the details. The time-averaged velocity magnitude contours for both cases were symmetric about the nozzle in the entire mold region. Also both cases were found to have stable flow pattern but the No-EMBr (Case 1) case had a weak upper recirculation region. In Case 3, the recirculation regions were very close to the jet and after they reach the nozzle the upper recirculation continues upward close to the SEN walls whereas the lower recirculation continues in the casting direction. In traditional double-roll flow pattern, which was seen in the No-EMBr case, the lower recirculation region extends deep into the mold before returning to the jet region, whereas in the conducting wall case it is

restricted close to jet with the flow below this region aligned to the casting direction.

The $\overline{w'w'}$ component of resolved Reynolds stresses in the mold region is presented in Figure 11. The resolved Reynolds stresses components, $\overline{w'w'}$, $\overline{v'v'}$ and $\overline{u'u'}$, were restricted to the jet region in the conducting wall case (Case 3), unlike the insulated wall case (Case 2) where the fluctuations extend into the upper mold region confirming an unstable flow pattern. This enhanced suppression in the mold region for the conducting wall case is attributed to the concentration of the high current density and Lorentz force to the region of

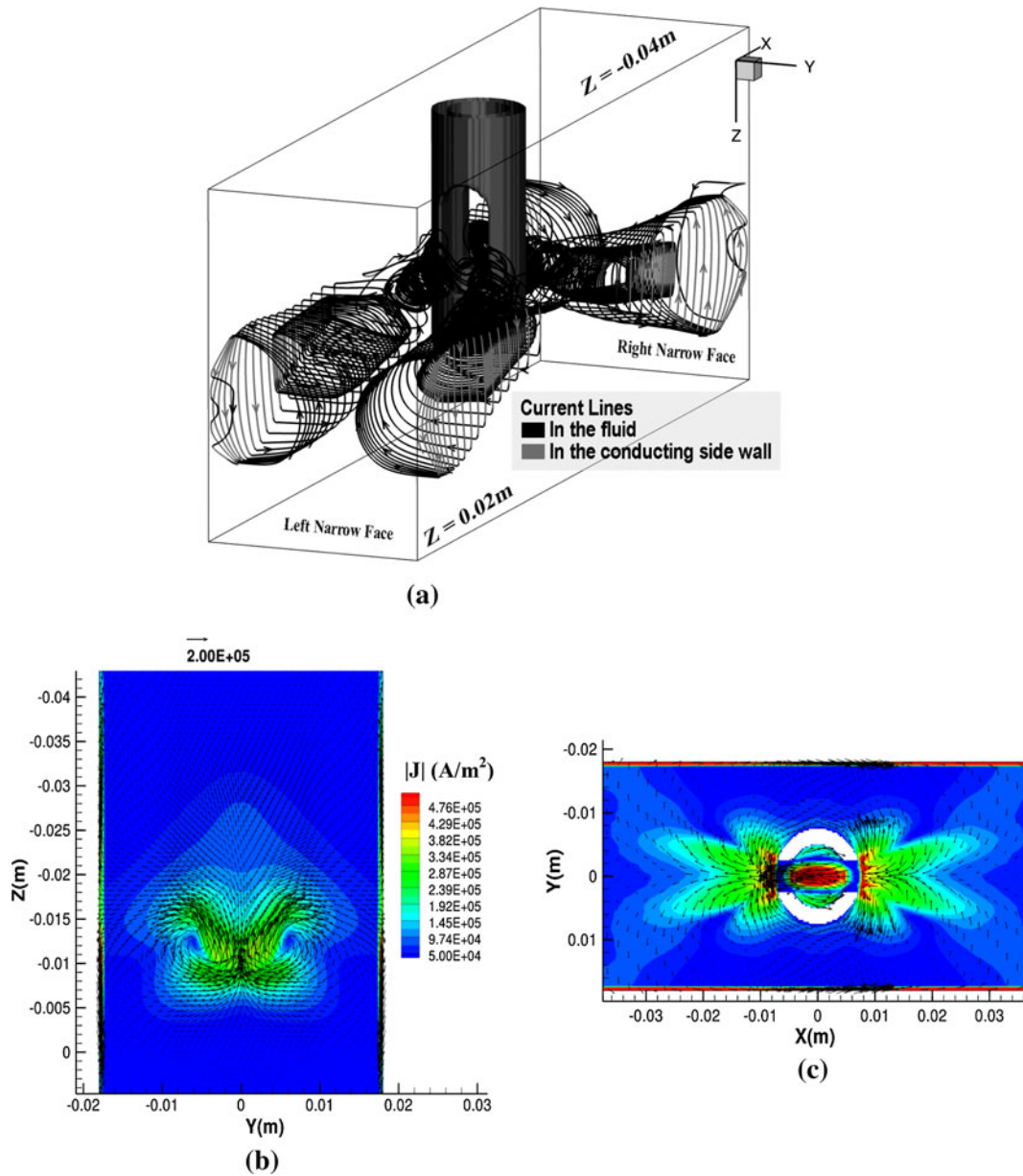


Fig. 8—(a) Current paths in the mold close to the nozzle ports. Contour plots of time-averaged current density magnitude on (b) vertical y - z plane at $x = -12\text{ mm}$ with vectors of J_y and J_z . (c) Horizontal x - y plane at $z = -10\text{ mm}$ with vectors of J_x and J_y .

strongest magnetic field. The resulting stable upper roll flow is beneficial for defect reduction.

3. Surface flow

Flow across the top surface is of critical importance to steel quality. Various defects form if the surface flow is either too fast or too slow. Figure 12 shows the variation of time-averaged horizontal surface velocity 1 mm below the free surface across the mold width, for Cases 1, 2, and 3. In general, the surface velocity in this GaInSn model is low because of the deep submergence depth. The No-EMBr case has the lowest surface velocity (max = 0.045 m/s) and might be susceptible to meniscus freezing.^[3] The EMBr with conducting wall case (Case 3) has the highest surface velocities, and the

time-averaged field is also symmetric on both sides. The maximum time-averaged surface velocity for the EMBr with insulated wall case (Case 2) lies between that of Cases 1 and 3, and variation across the mold width for this case was asymmetric about the SEN.

The EMBr flow with conducting walls also has the beneficial effect of lowering the TKE at the surface, as shown in Figure 13. The extremely high and asymmetric TKE at the surface for the insulated wall case suggests large-scale level fluctuations and associated quality problems. Thus, the effect of the shell conductivity should be considered to accurately study the mold flow under the influence of applied magnetic fields, especially when considering transient phenomena.

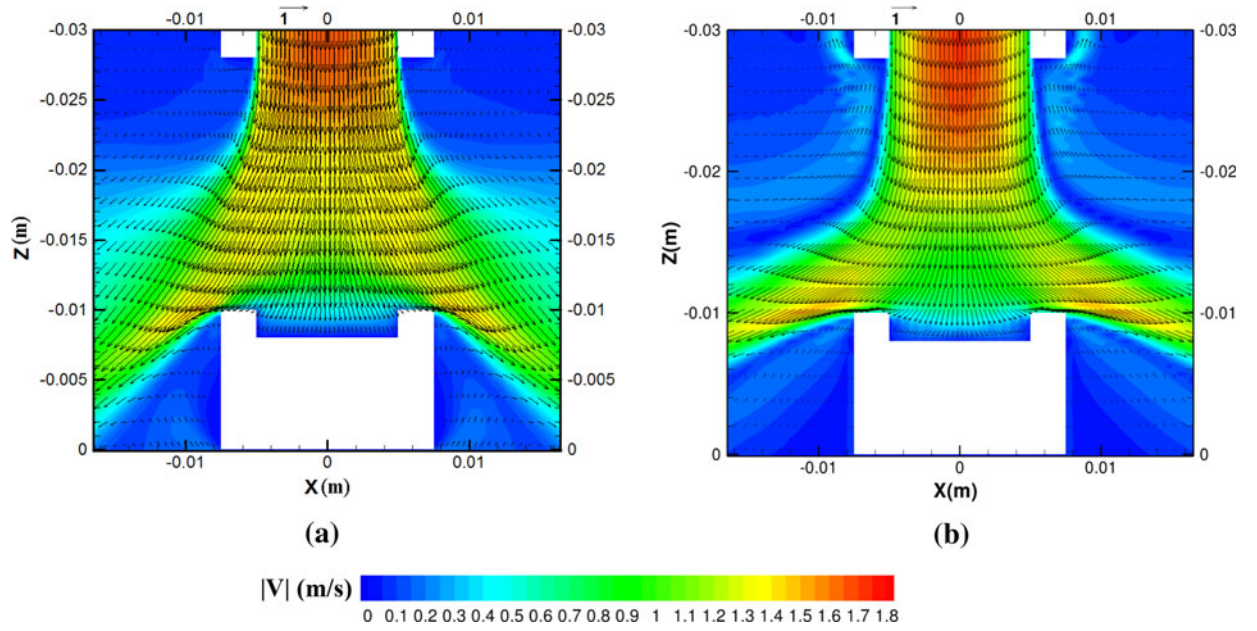


Fig. 9—Time-averaged velocity magnitude contours and vectors near nozzle bottom in different cases (66 pct of vectors are skipped for clarity).

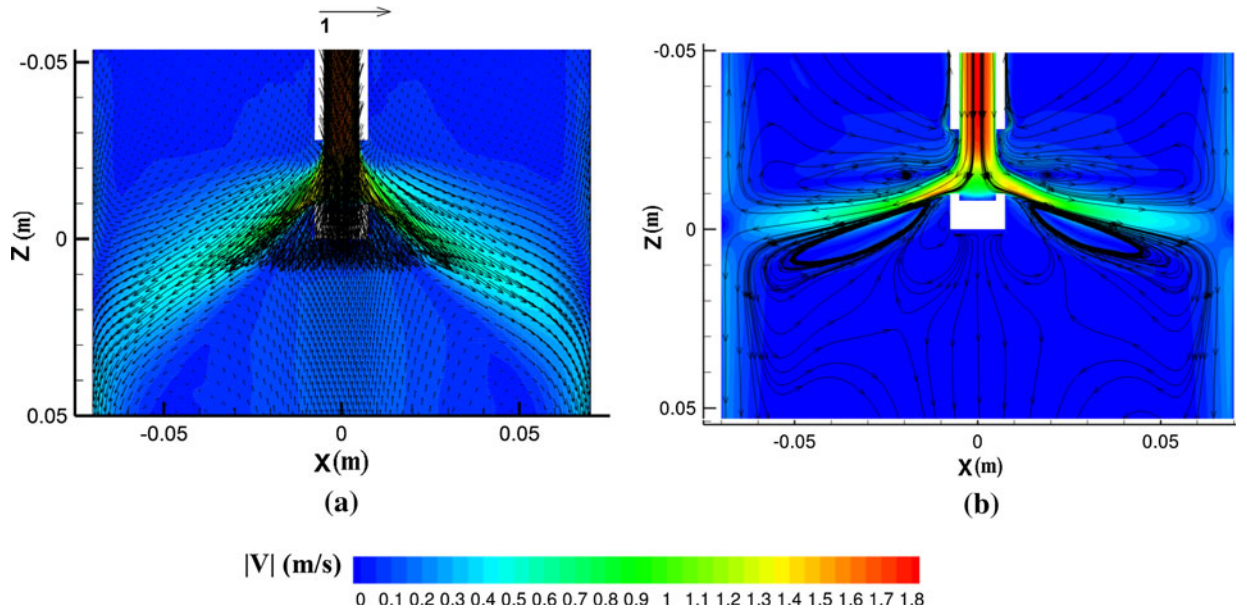


Fig. 10—Contours of time-averaged velocity magnitude and vectors/streamlines at mold midplane for (a) no-EMBr case^[3] and (b) EMBr case with conducting walls (83 pct of vectors are skipped for clarity).

V. RESULTS FOR THE REAL CASTER

A. Transient Results

1. Effect of EMBr on transient flow

Having validated the CUFLOW model, it was applied to simulate transient flow in a realistic full-scale commercial caster. For both the No-EMBr (Case 4) and the EMBr (Case 5) cases, Figure 14 shows instantaneous contours of velocity magnitude at two different times, at intervals of one second. It can be seen that with no EMBr, the transient flow field is dominated by small-scale fluctuations. The application of EMBr damps most

of the small-scale fluctuations and deflects the jets upward. These deflected jets were reasonably stable and the long time fluctuations were comparable with the No-EMBr case. The flow below the jet region quickly aligns to the casting direction, and the lower roll was restricted to a small, elongated recirculation loop just below the jet.

It has been previously seen that an applied magnetic field preferentially damps the transient flow fluctuations parallel to its direction.^[27] Figure 15 shows the computed time history of two fluctuating velocity components (y in the thickness direction and z in the casting

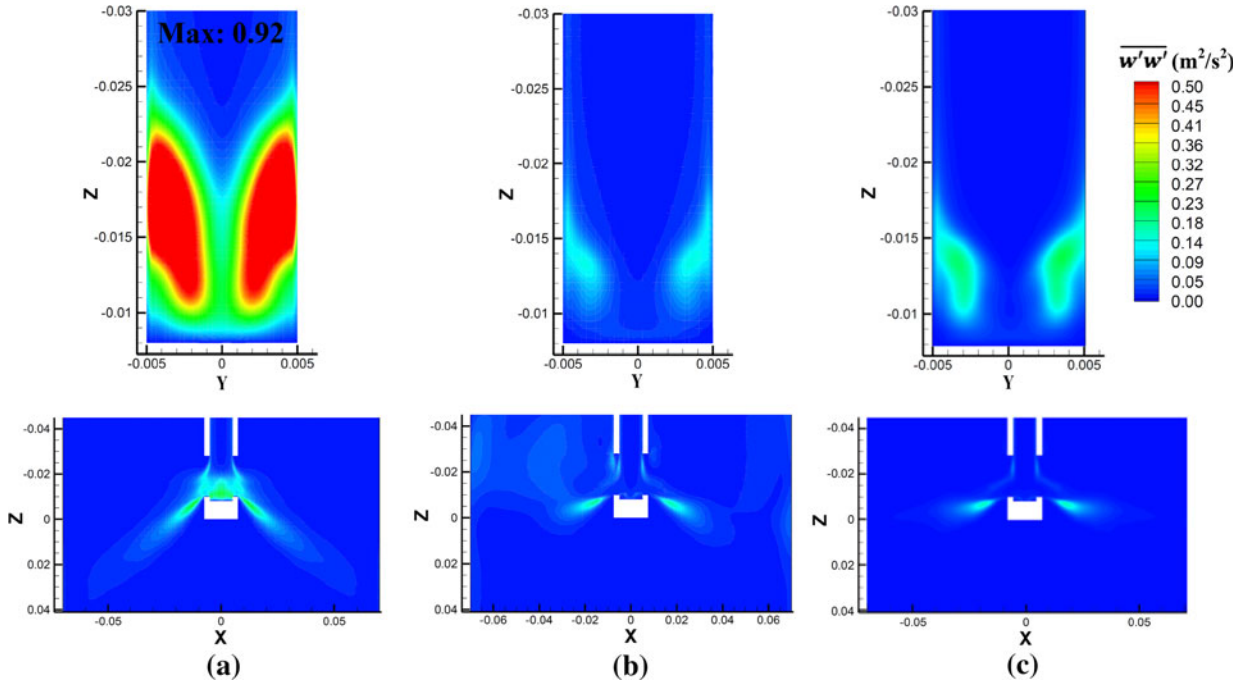


Fig. 11— $\overline{w'w'}$ component of resolved Reynolds stresses at mold mid-planes between wide faces (below) and between narrow faces inside nozzle (above). (a) No-EMBr,^[3] (b) EMBr with insulated walls^[3] and (c) EMBr with conducting walls (all axes in meters).

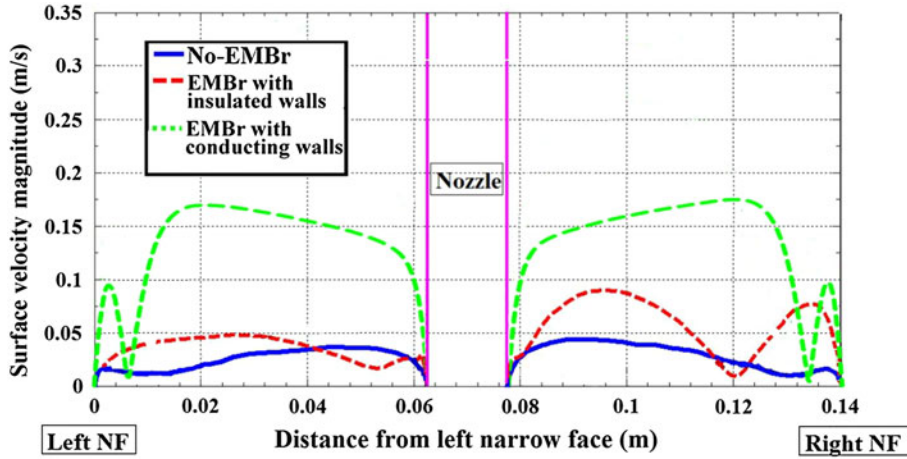


Fig. 12—Time-averaged horizontal velocity at the surface plotted against distance from left narrow face.

direction) at two points P1 (center of SEN bottom) and P2 (near port exit) as previously indicated in Figure 1 for the two cases, with and without the magnetic field. The high variation in V'_z and V'_y at P1 with no EMBr indicates the presence of swirling flow in the nozzle bottom. The frequency of the alternating direction of the swirl can be approximated, from the time history of V'_y in Figure 15(a), to be about 1.5 Hz. With EMBr, the low velocity fluctuations at P1 indicate very little swirl in the nozzle which results in a smoother jet with less high-frequency turbulent fluctuations. The time history at P2 shows highly anisotropic suppression of turbulence, as the thickness-direction V'_y component is damped more by the magnetic field.

2. Free surface fluctuations and effect of scaling

The profile of the steel surface level (Z_{sur}) and its fluctuations are of critical importance to the steel quality as mold slag entrainment and surface defects can occur if the fluctuations are too strong. The surface level can be approximated using the pressure method in Eq. [14]^[34] which gives an estimate of the liquid surface variation using a potential energy balance.

$$Z_{\text{sur}} = \frac{p - p_{\text{mean}}}{\rho_{\text{steel}} g} \quad [14]$$

The average pressure (p_{mean}) in the current study was calculated on the horizontal line along the top surface

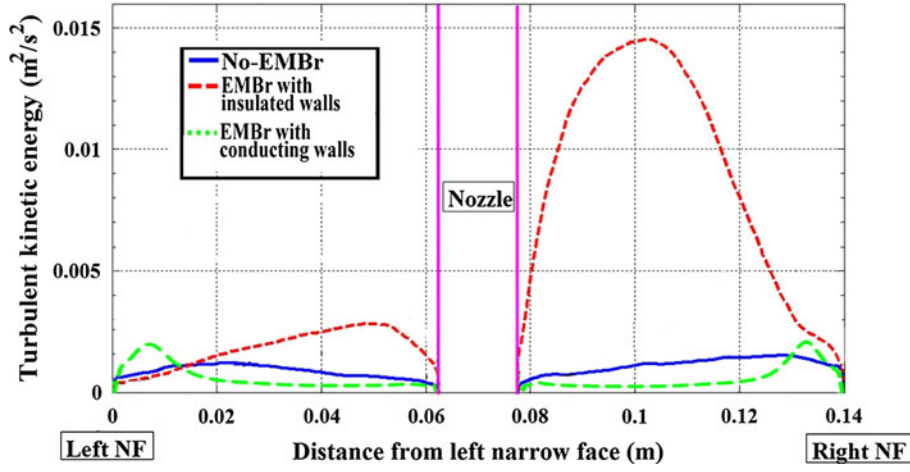


Fig. 13—Resolved turbulent kinetic energy at the surface plotted against distance from left narrow face.

on midplane between the wide faces with g taken as 9.81 m/s^2 . Figure 16 shows three typical instantaneous surface-level profiles, with a 0.5 seconds moving time average, at three instances separated by 5 seconds each. With no EMBr, the surface level remains almost horizontal with higher levels ($\sim 0.5 \text{ mm}$) close to the NF and SEN. The level variation in the EMBr case was greater, because of the increase in momentum, both close to the NF ($\sim 2.7 \text{ mm}$) and to the SEN ($\sim 1.7 \text{ mm}$). The time variation of the level is plotted, at P3 and P4, and is shown in Figure 17. Point P3 is at the midpoint between the NF and the SEN; and P4 is close to the NF as indicated in Figure 1. The No-EMBr case at both locations is found to be stable with only small scale fluctuations. The EMBr case at P3 has small fluctuations with oscillation amplitude of $\sim 0.5 \text{ mm}$; whereas at P4 there was a periodic oscillation with amplitude of 3 mm and frequency of $\sim 0.2 \text{ Hz}$.

In order to compare the level fluctuations predicted by the GaInSn model with the real caster, they must be scaled. The obvious scaling method is to multiply the scale-model level fluctuations by the geometric length scaling factor ($= 6$). However, a better scaling method is to calculate the ratio of the Froude numbers in the two casters, and rearrange to give the following length scaling factor.

$$\frac{L_R}{L_S} = \frac{Fr_S}{Fr_R} \left(\frac{V_R}{V_S} \right)^2 = 2.974 \quad [15]$$

where L is the characteristic length scale, V the characteristic velocity and the subscripts “S” and “R” represent the GaInSn scaled model and the real caster, respectively. Figure 17 compares the scaled level fluctuations using both scaling methods, with the real caster history, for Case 3 at points P3 and P4. The geometric scaling method overpredicts the average surface-level position and its fluctuations in the real caster (Case 5) at both locations. However, the Froude-number based scaling factor matches the calculated level fluctuations in the real caster very closely. This indicates that the surface-level fluctuations in scaled models can

accurately predict behavior in the real caster, if they are scaled based on the Froude-number relationship in Eq. [15].

B. Time-Averaged Results

1. Nozzle flow

Figure 18 shows the contours of time-averaged velocity magnitude along with velocity vectors, for the No-EMBr and the EMBr cases. As expected, both contour plots are symmetric about the nozzle centerline indicating adequate time averaging. The jets in the No-EMBr case exit with a steeper angle (30 deg down) and spread more compared with the jets in the EMBr case (10 deg down). Figure 19 shows the variation of time-averaged velocity magnitude at the vertical line of the midplane of the nozzle port exits. The No-EMBr case has a lower time-averaged velocity magnitude at the top of the nozzle port exit and the value steadily rises around 30 mm from the top. The EMBr case also has a low time-averaged velocity magnitude at the top of the nozzle port exit but the value remains low more than halfway ($\sim 60 \text{ mm}$) down the port height. The magnitude then steadily rises reaching approximately the same maximum value as the No-EMBr case. This indicates that there are flatter (in the Z-direction) and thicker (in the Y-direction) jets exiting the nozzle ports in the presence of the EMBr field.

The suppression of turbulence in the nozzle by the magnetic field is shown in Figure 20, where the TKE is plotted with distance down the nozzle port. The variation is symmetric for both cases, but the maximum value with EMBr is lower by a factor of approximately five. The current EMBr position applies the maximum magnetic field strength directly across the nozzle ports, which causes high suppression of both the turbulent fluctuations and the swirl in the SEN well (Figure 15). The contours of TKE inside the nozzle in the y - z midplane also aid in visualizing the suppression of alternating swirl in the nozzle as shown in Figure 21. The No-EMBr case has high TKE values inside the nozzle which were considerably reduced in the presence

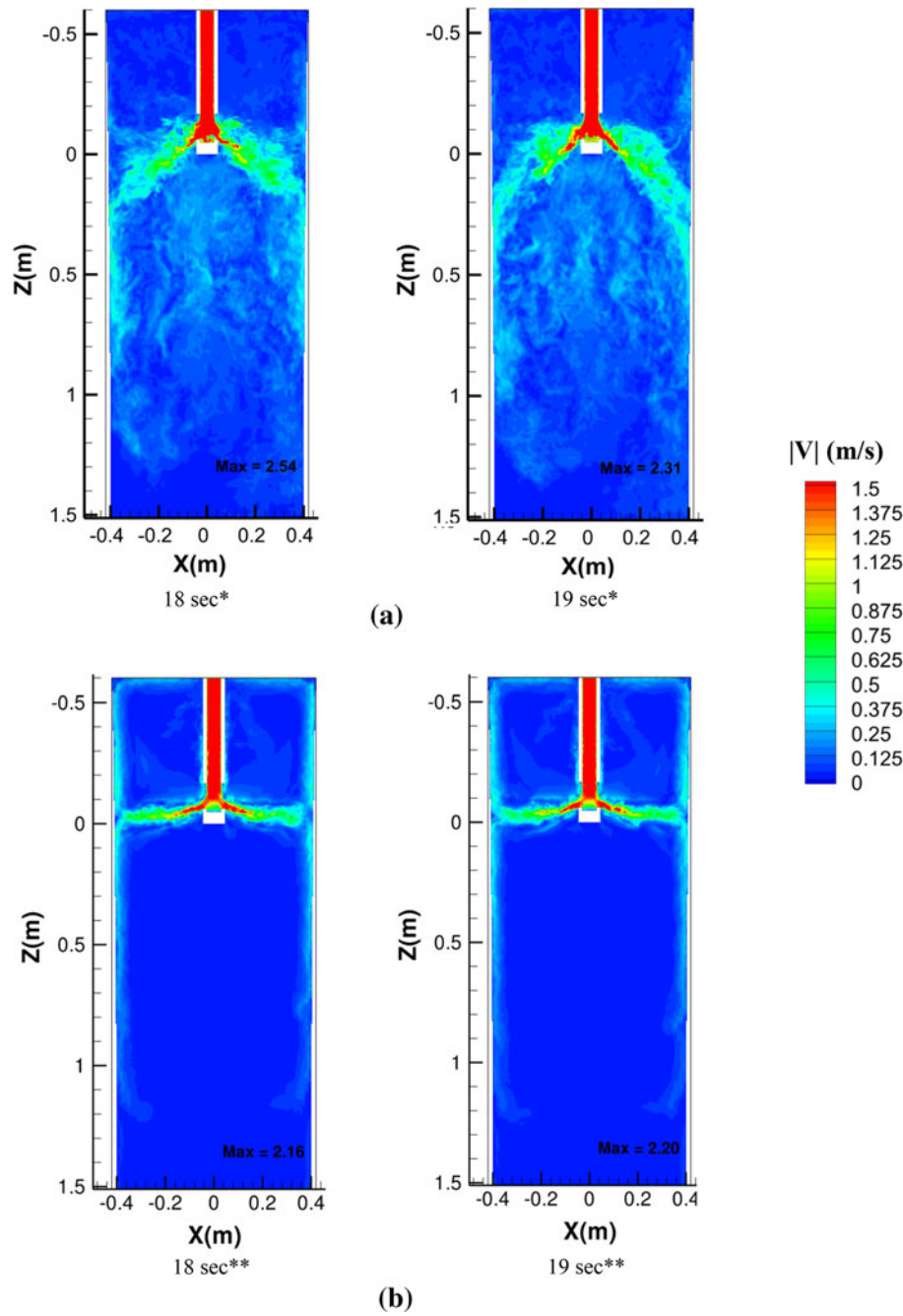


Fig. 14—Instantaneous velocity magnitude for the real caster cases. (a) No-EMBr and (b) with EMBr (*time from start of simulation, **time after switching on EMBr).

of the magnetic field as expected. The vectors of time-averaged velocity field in Figure 21 show the structure of the swirling flow at the nozzle bottom. In the No-EMBr case, the swirls at the SEN bottom are bigger and also have stronger velocities compared with the EMBr case. Furthermore, another important effect of the EMBr field on the nozzle flow is seen in the time-averaged velocity profile in the Y-direction (Figure 21) which becomes considerably flat in the presence of the EMBr field. The diagonal components of the Reynolds stress tensors are not shown for Cases 4 and 5 to avoid redundancy as they were qualitatively similar to the Cases 1 and 3 (Figure 11) of the GaInSn model.

2. Mold flow

Figure 22 shows the contours of time-averaged velocity magnitude in the mold region with streamlines for the No-EMBr and EMBr cases. Time averaging over a long time shows the double roll flow pattern present with a weaker upper roll. The mean mold flow pattern for the EMBr case is expected to be the same as the GaInSn model EMBr case with conducting walls because Stuart number similarity was used to scale the process parameters. Application of the EMBr deflects the jets upward resulting in an increased impinging velocity at higher positions on the NFs. The deflected jets strengthen the upper roll and create a similar stable

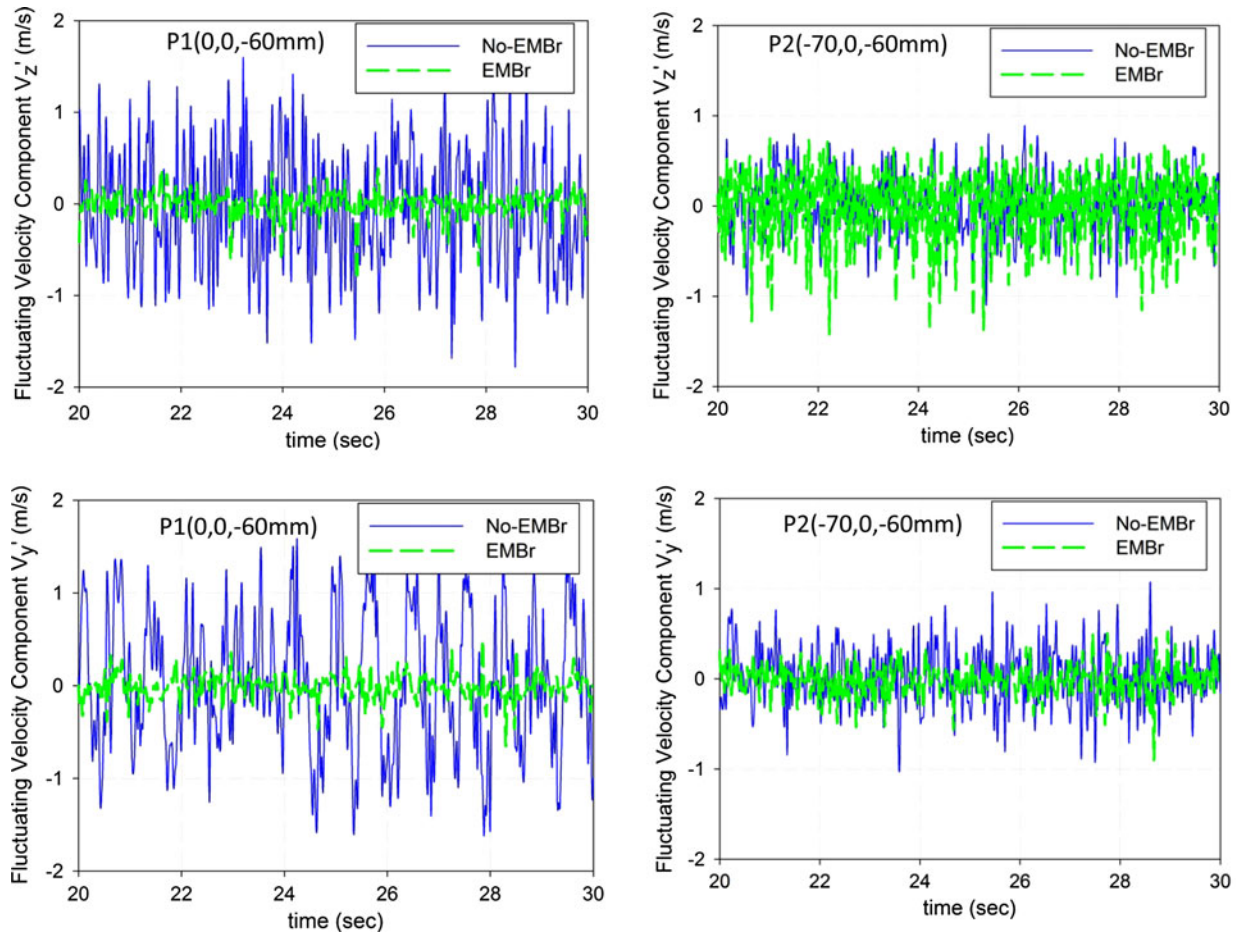


Fig. 15—Time variation of components of the fluctuating velocity plotted for the real caster cases at (a) P1 and (b) P2.

flow pattern to the EMBr with conducting walls case for the GaInSn model. The two small recirculation regions, immediately above and below the jets, as seen in the Case 3, were also observed in the real caster with EMBr case. In addition to this small recirculation region, there were two other recirculation loops in the upper mold region. The jet rising along the NF and the stream rising along the SEN wall form the two loops with opposite circulation.

The mold flow below the jet region critically affects the penetration depth and entrapment chances of the bubbles and entrained particles. Figure 23 shows variation of time-averaged vertical velocity along three horizontal lines, on the midplane between the wide faces, below the jet region. The downward velocity is always the highest near the NFs, and decreases with depth down the caster. The No-EMBr case has higher downward velocity close to the NFs compared with the case with the EMBr field. However, the major difference can be seen further away from the NFs where the flow is completely reversed with the application of the EMBr. Without EMBr, the flow in the central region is upward, *i.e.*, moving toward the nozzle region, whereas the flow with EMBr aligns with the casting direction. In the EMBr flow field, the downward velocities away from the NFs are small and comparable with the casting velocity

(shown in the figure). These low velocities in the EMBr case should be beneficial for the reduction in penetration and entrapment of bubbles, and detrimental nonmetallic particles.

3. Surface flow

Figure 24 compares the time-averaged surface velocity magnitudes, 6 mm below the free surface (which is six times the distance plotted for the GaInSn model) across the mold width, between the No-EMBr and the EMBr cases. The time-averaged surface velocity magnitude toward the SEN for the EMBr case was much higher (maximum of 0.25 m/s in the real caster) compared with the No-EMBr case (maximum of 0.07 m/s), because of the stronger flow up the NF walls. The sudden drop to zero surface speed found very close to the NF, for the EMBr cases, indicates a switch in the direction of the surface velocity. This is due to a small recirculating region that forms near each NF, because of the concave shell profile at the edge of the fluid domain.

The stability of the surface is also an important factor in determining the steel quality. Figure 25 shows the variation of TKE along the mold surface on the midplane between the wide faces for the No-EMBr and the EMBr case. Both cases have TKE of the same order of magnitude along the surface. The EMBr case

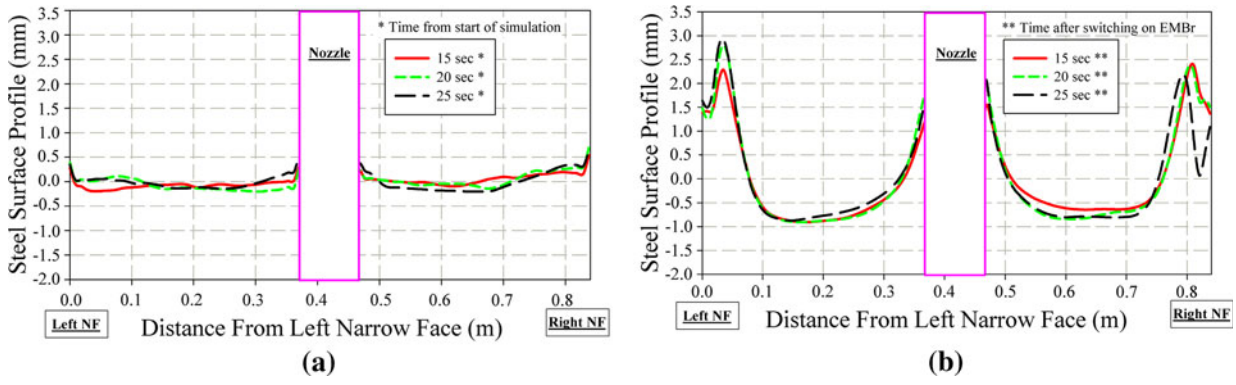


Fig. 16—Instantaneous mold surface-level prediction at three instances for the real caster cases (a) no-EMBr and (b) with EMBr.

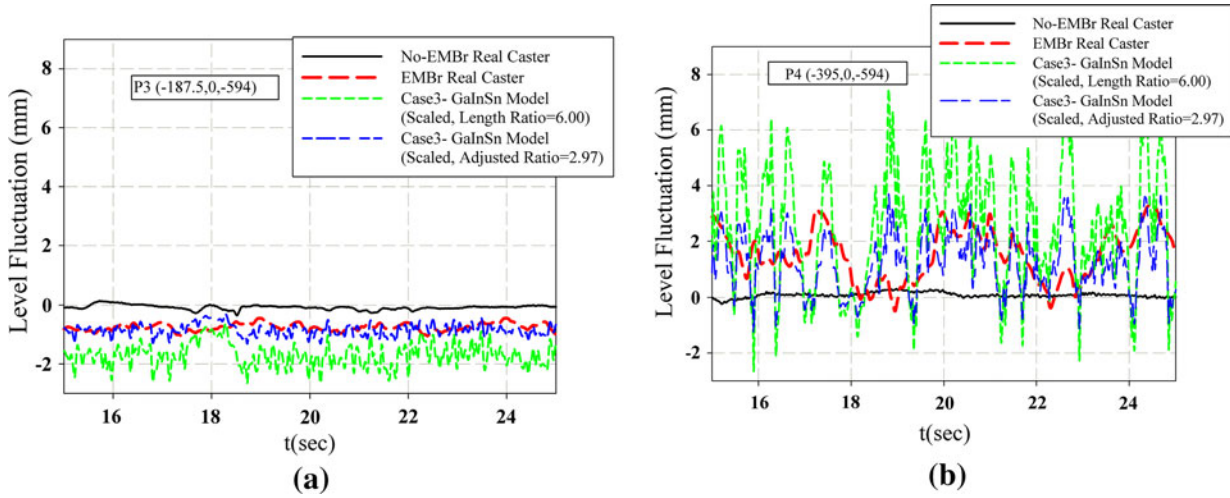


Fig. 17—Mold surface-level histories for the real caster cases and GaInSn model case 3 with scaled surface level (a) midway between SEN and narrow face at P3 and (b) near narrow face at P4.

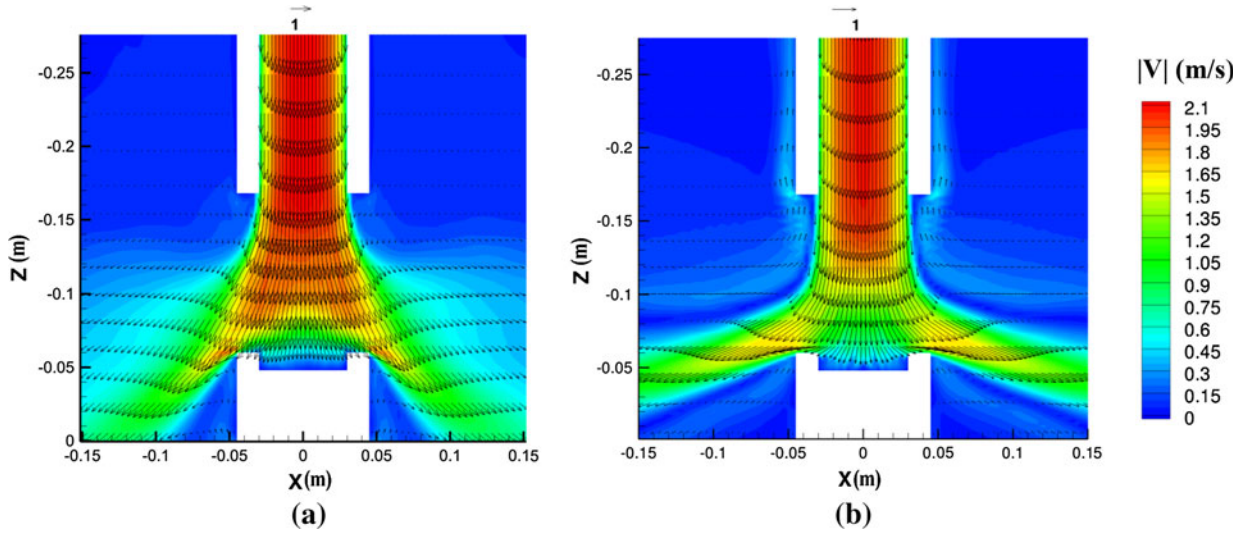


Fig. 18—Time-averaged velocity magnitude contours and vectors near nozzle bottom for the real caster cases. (a) No-EMBr and (b) with EMBr (83 pct of vectors are skipped for clarity).

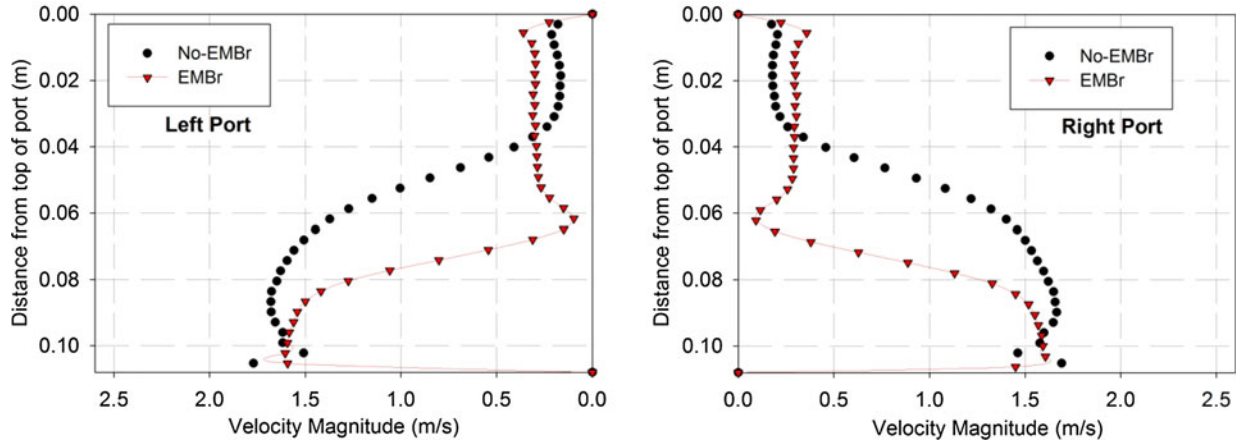


Fig. 19—Time-averaged velocity magnitude plotted along the port midplane vertical line for the real caster cases.

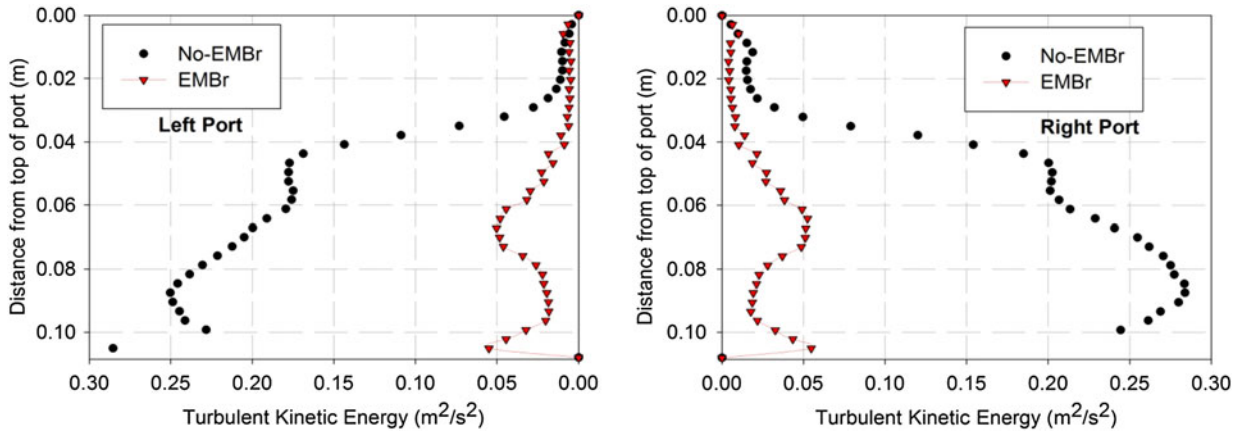


Fig. 20—Resolved turbulent kinetic energy plotted along the port midplane vertical line for the real caster cases.

has definite peaks of high TKE close to the NF ($\sim 0.005 \text{ m}^2/\text{s}^2$) and SEN ($\sim 0.002 \text{ m}^2/\text{s}^2$), whereas with no EMBr, the variation along the width was gradual.

4. Effects of scaling

The flow fields predicted for the 1/6 scale-model (Case 3) and the real caster (Case 5) are very similar, even though the dimensions differ greatly. The surface-level profiles could be matched using appropriate Froude-number based scaling. To further study the validity of using Stuart number similarity for scaling EMBr cases, velocities in the GaInSn model were scaled by the ratio of the characteristic velocities in the real caster and the GaInSn model ($1.7/1.4 = 1.21$, from the inlet velocities in the jet region is shown in Figure 23(b) along one of the horizontal lines ($z = 0.40 \text{ m}$, $y = 0$). The variation of the vertical velocities across the width agrees well with the corresponding real caster curve after shifting and scaling the axes to accommodate for the shell thickness on the NFs of the real caster. Scaled surface velocities are also compared with the calculated values in the real caster and are seen to agree (Figure 24). The higher surface velocity in the real caster is an effect of the tapered solidifying shell. It has been shown in a previous

study that the tapered shell, and the consequent reduction in cross-section area, deflects more fluid upward into the upper recirculation region, leading to the increased surface velocity.^[34]

The agreement between the scaled velocities for Case 3 and the velocities for Case 5 is shown more completely also in Figure 26. It can be seen that both the flow patterns as well as the velocity magnitudes match well over the entire mold.

VI. SUMMARY AND CONCLUSIONS

LES of flow in a full-scale steel caster with the effects of a ruler magnetic field and conducting steel shell were performed. The computational approach was first validated with measurements made in a GaInSn physical model^[13] and also with simulations with an insulated electrical boundary condition. The GaInSn model was then scaled to correspond with a full-sized caster and was studied at conditions similar to industrial operations. However, in order to compare the results with the GaInSn model, the submergence depth was kept proportionally the same as the GaInSn model which was deeper than typical industrial conditions.

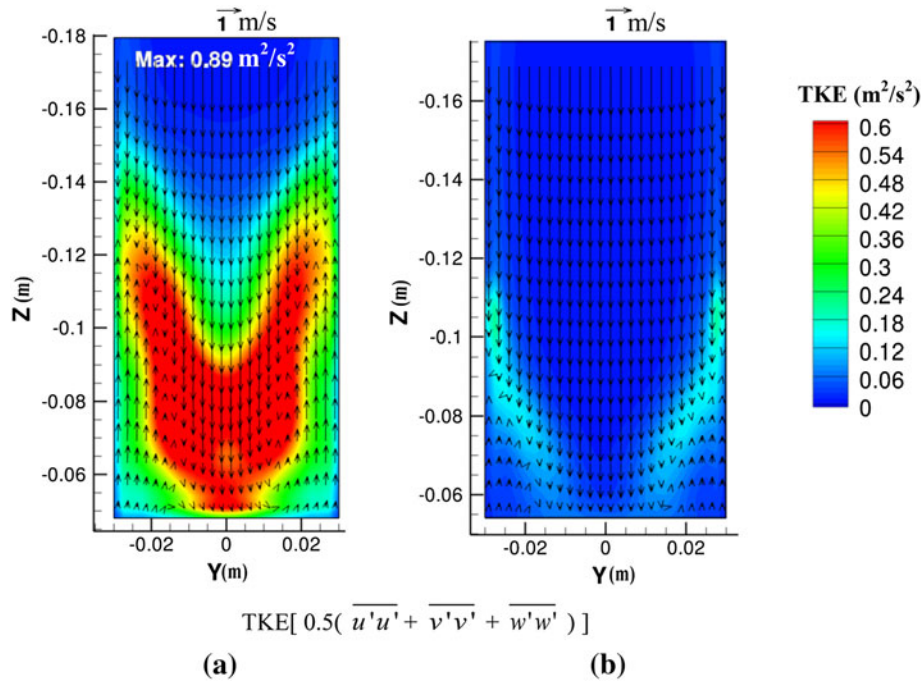


Fig. 21—Contours of turbulent kinetic energy with vectors of time-averaged velocity components (V_z and V_y) at mold mid-planes between narrow faces inside nozzle for the real caster cases (50 pct of vectors are skipped for clarity).

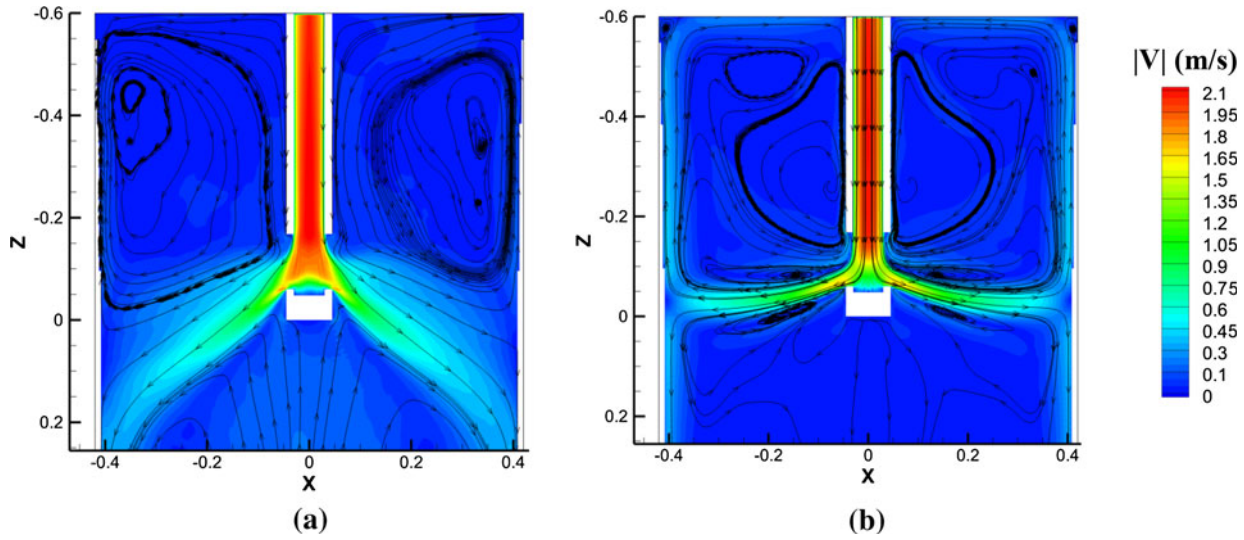


Fig. 22—Time-averaged velocity magnitude contours and streamlines at mold midplane for the real caster cases. (a) No-EMBr and (b) with EMBr (all axes in meters).

The large-scale jet wobble and transient asymmetric flow in the mold with insulated walls was not found with conducting walls. With a realistic conducting shell for otherwise identical conditions, the flow was stable, and it quickly achieved a symmetrical flow pattern, which featured three counter-rotating loops in the upper region and top surface flow toward the SEN. The turbulence due to Reynolds stresses were suppressed in the presence of the applied magnetic field. The suppression in the conducting shell case was, however, found to be lower in the nozzle region. Also, with the conducting shell the

Reynolds stresses were restricted only to the jet region in the mold. Thus, it is essential to include the effect of the conducting shell when studying transient mold flow with a magnetic field.

Relative to the case with no EMBr field, the ruler magnetic brake across the nozzle deflects the jets upward, from approximately 30 deg down to only 10 deg down. This strengthens the flow in the upper region and increases the top surface velocity from NF to SEN, from 0.07 to 0.25 m/s in the real caster. The weaker upper recirculation region without EMBr

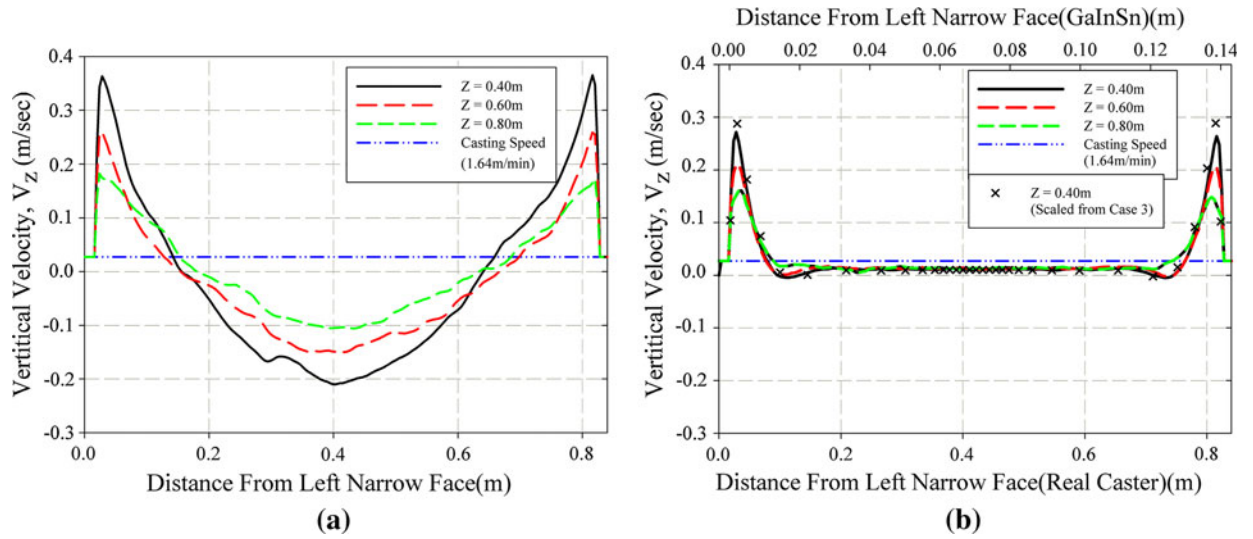


Fig. 23—Time-averaged vertical velocity (V_z) at three vertical locations in the midplane parallel to the mold wide face plotted against distance from narrow face. (a) Real caster no-EMBr case and (b) real caster with EMBr case and GaInSn model EMBr with conducting wall case (scaled velocity).

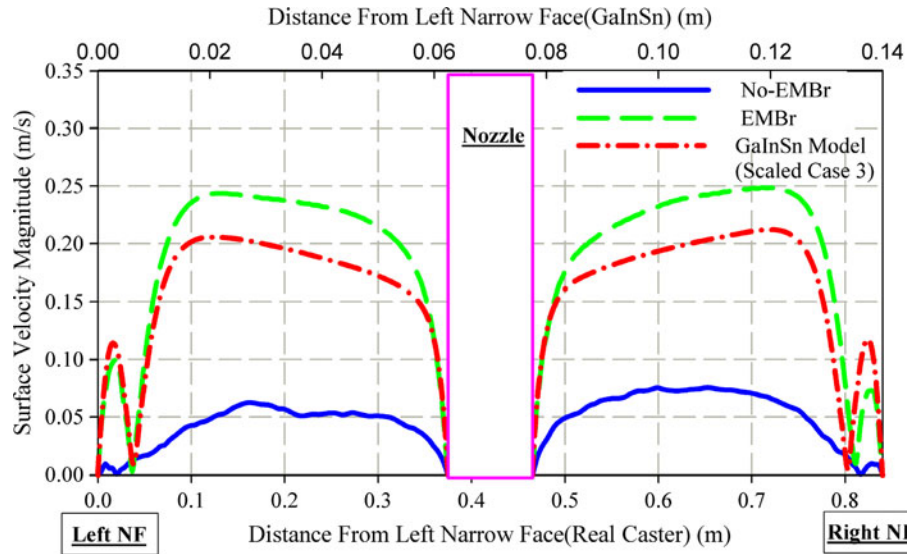


Fig. 24—Time-averaged horizontal velocity at the surface plotted against distance from narrow face for the real caster cases and the GaInSn model with conducting wall case (scaled velocity).

becomes more complex with the application of the ruler magnetic brake, with three distinct recirculation loops, featuring upward flows along both the NF and the SEN. The momentum from these flows raises the surface level near the NF and SEN, and generates higher level fluctuations in these two regions. The lower recirculation region becomes a very small elongated loop just below the jet, which is similar to a small loop that forms just above the jet. Flow below this small recirculation loop aligns quickly to the casting direction. These lower downward velocities with EMBr should be beneficial for lessening the penetration and entrapment of bubbles and inclusion particles.

The Stuart number similarity criterion employed in the current study enables a close match of both the time-averaged mold flow pattern (qualitative) and velocities (quantitative) between the 1/6-scale model and the real caster. The scaled surface-level profile and its time fluctuations were matched as well, when using a scaling factor based on the ratio of the Froude numbers. Simply scaling the GaInSn model predictions using the geometric scale factor of 6 resulted in an overprediction of the surface-level profile and fluctuations, because the Froude number of this scaled model was larger than that of the real caster. This Froude-number based scaling method avoids the need to

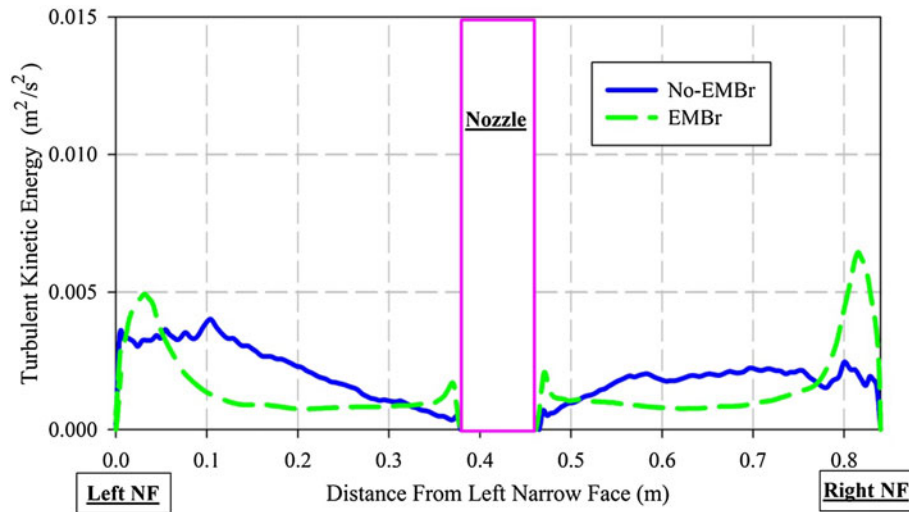


Fig. 25—Resolved turbulent kinetic energy at the surface plotted against distance from the left narrow face for the real caster cases.

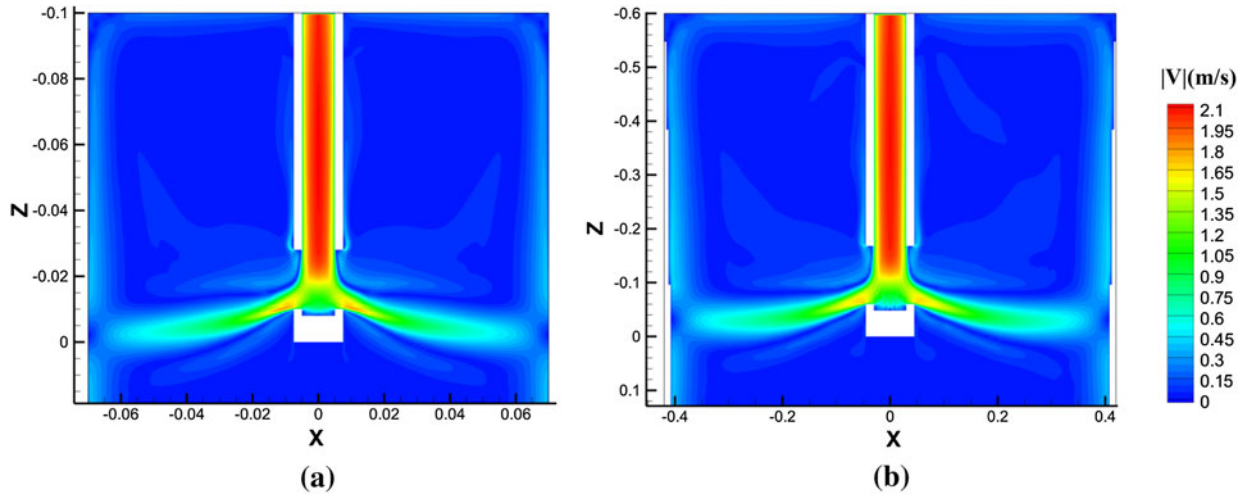


Fig. 26—Time-averaged velocity magnitude contour on midplane between wide faces for (a) GaInSn model conducting wall case with scaled velocity magnitude and (b) real caster with EMBr case (all axes in meters).

maintain both Froude number and Stuart number similarity conditions simultaneously when choosing operating conditions for a scaled model caster with EMBr.

ACKNOWLEDGMENTS

The current study was supported by the National Science Foundation Grant CMMI 11-30882 and the Continuous Casting Consortium. The authors are also grateful to K. Timmel, S. Eckert, and G. Gerbeth from the MHD Department, Forschungszentrum Dresden-Rossendorf (FZD), Dresden, Germany for providing the velocity measurement database of the GaInSn model experiment with conducting side walls.

REFERENCES

1. *World Steel in Figures 2012*, World Steel Association, Brussels, Belgium, 2012.
2. R. Chaudhary and B.G. Thomas: *6th International Conference on Electromagnetic Processing of Materials EPM*, 2009.
3. R. Chaudhary, B.G. Thomas, and S.P. Vanka: *Metall. Mater. Trans. B*, 2012, vol. 43B, pp. 532–53.
4. C. Zhang, S. Eckert, and G. Gerbeth: *J. Fluid Mech.*, 2012, vol. 575, pp. 57–82.
5. K. Cukierski and B.G. Thomas: *Metall. Mater. Trans. B*, 2008, vol. 39B, pp. 94–107.
6. D. Kim, W. Kim, and K. Cho: *ISIJ Int.*, 2000, vol. 40, pp. 670–76.
7. K. Takatani, K. Nakai, N. Kasai, T. Watanabe, and H. Nakajima: *ISIJ Int.*, 1989, vol. 29, pp. 1063–68.
8. M.Y. Ha, H.G. Lee, and S.H. Seong: *J. Mater. Process. Technol.*, 2003, vol. 133, pp. 322–39.
9. H. Harada, T. Toh, T. Ishii, K. Kaneko, and E. Takeuchi: *ISIJ Int.*, 2001, vol. 41, pp. 1236–44.
10. B. Li, T. Okane, and T. Umeda: *Metall. Mater. Trans. B*, 2000, vol. 31B, pp. 1491–1503.

11. A. Idogawa, M. Sugizawa, S. Takeuchi, K. Sorimachi, and T. Fujii: *Mater. Sci. Eng. A*, 1993, vol. 173, pp. 293–97.
12. K. Timmel, X. Miao, S. Eckert, D. Lucas, and G. Gerbeth: *Magnetohydrodynamics*, 2010, vol. 46, pp. 437–48.
13. K. Timmel, S. Eckert, and G. Gerbeth: *Metall. Mater. Trans. B*, 2011, vol. 42B, pp. 68–80.
14. X. Miao, K. Timmel, D. Lucas, S. Ren, Z. Eckert, and G. Gerbeth: *Metall. Mater. Trans. B*, 2012, vol. 43B, pp. 954–72.
15. B.G. Thomas and L. Zhang: *ISIJ Int.*, 2001, vol. 41, pp. 1181–93.
16. R. Chaudhary, C. Ji, B.G. Thomas, and S.P. Vanka: *Metall. Mater. Trans. B*, 2011, vol. 42B, pp. 987–1007.
17. Z. Qian, Y. Wu, B. Li, and J. He: *ISIJ Int.*, 2002, vol. 42, pp. 1259–65.
18. R. Kageyama and J.W. Evans: *ISIJ Int.*, 2002, vol. 42, pp. 163–70.
19. Y. Miki and S. Takeuchi: *ISIJ Int.*, 2003, vol. 43, pp. 1548–55.
20. T. Ishii, S.S. Sazhin, and M. Makhlouf: *Ironmak. Steelmak.*, 1996, vol. 23, pp. 267–72.
21. Y. Hwang, P. Cha, H.-S. Nam, K.-H. Moon, and J.-K. Yoon: *ISIJ Int.*, 1997, vol. 37, pp. 659–67.
22. P.H. Dauby: *Int. J. Metall.*, 2012, vol. 109, pp. 113–36.
23. Q. Yuan, B.G. Thomas, and S.P. Vanka: *Metall. Mater. Trans. B*, 2004, vol. 35B, pp. 685–702.
24. R. Chaudhary, S.P. Vanka, and B.G. Thomas: *Phys. Fluids*, 2010, vol. 22, pp. 075102–15.
25. R. Chaudhary, A.F. Shinn, S.P. Vanka, and B.G. Thomas: *Comput. Fluids*, 2011, vol. 51, pp. 100–14.
26. H. Kobayashi: *Phys. Fluids*, 2008, vol. 20, pp. 015102–14.
27. R. Moreau: *Magnetohydrodynamics*, Kluwer, Norwell, MA, 1990, pp. 110–64.
28. A.F. Shinn and S.P. Vanka: *J. Turbomach.*, 2013, vol. 135, pp. 011004–16.
29. A.F. Shinn: *Large Eddy Simulations of Turbulent Flows on Graphics Processing Units: Application to Film-Cooling Flows*, University of Illinois at Urbana-Champaign, Urbana, 2011.
30. J. Smagorinsky: *Annu. Weather Rev.*, 1963, vol. 96, pp. 99–164.
31. F. Nicoud and F. Ducros: *Flow Turbul. Combust.*, 1999, vol. 62, pp. 183–200.
32. H. Kobayashi: *Phys. Fluids*, 2006, vol. 18, p. 045107.
33. J. Iwasaki and B.G. Thomas: *Supplemental Proceedings*, John Wiley & Sons, Inc., New York, 2012, pp. 355–62.
34. R. Chaudhary, B.T. Rietow, and B.G. Thomas: *Mater. Sci. Technol.*, AIST/TMS, Pittsburgh, PA, 2009, pp. 1090–1101.
35. H. Werner and H. Wengle: *8th Symposium on Turbulent Shear Flows*, 1991, pp. 155–68.
36. A. Vorobev, O. Zikanov, P.A. Davidson, and B. Knaepen: *Phys. Fluids*, 2005, vol. 17, pp. 125105–16.